Dielectric Shimming

Optimization Techniques for Dielectric Pads in MRI

M. M. J. Gerlach

Technische Universiteit Delft

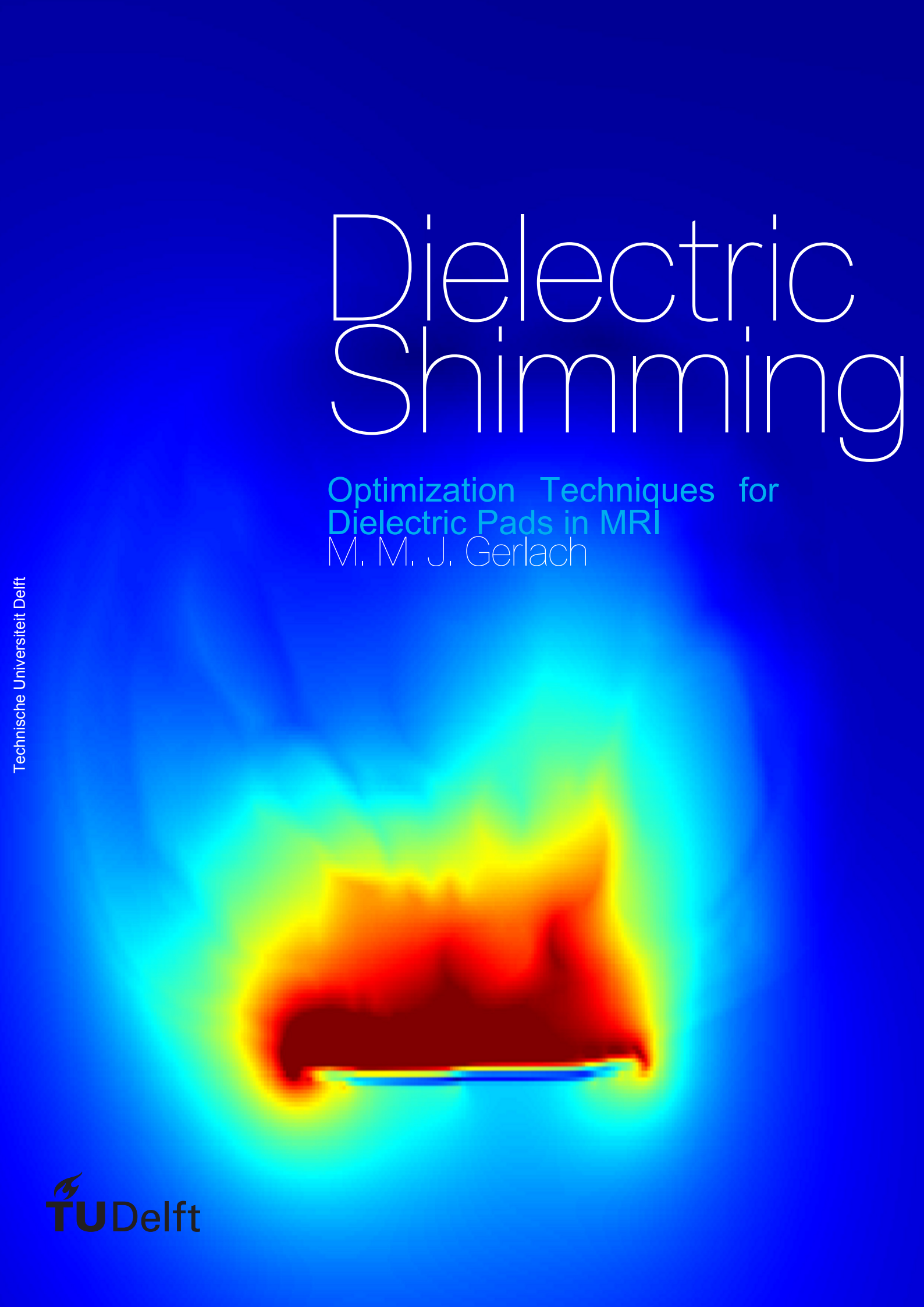

TU Delft

Dielectric Shimming

Optimization Techniques for Dielectric Pads in MRI

by

M. M. J. Gerlach

to obtain the degree of Master of Science
at the Delft University of Technology,
to be defended publicly on Friday July 29, 2016 at 10:45 AM.

Student number:	4003993	
Project duration:	October 12, 2015 – July 29, 2016	
Thesis committee:	Prof. dr. ir. A. -J. van der Veen,	TU Delft, Responsible Professor
	Dr. ir. R. F. Remis,	TU Delft, supervisor
	Prof. dr. ir. A. G. Webb,	LUMC
	Ir. J. H. F. van Gemert,	TU Delft

TU Delft

Abstract

Dielectric shimming is proven to be very useful in increasing the homogeneity of the B_1^+ field in high field MRI. Current optimization and design techniques for dielectric pad parameters are slow. The goal of this thesis is to find a fast and accurate pad design and optimization technique. Two new techniques are proposed. The first, a method that simply uses inspection by solving the forward problem in a relatively fast way. The other proposed technique follows a more analytical approach to find the optimal permittivity and conductivity of a pad in a couple of iterative steps with a Gauss-Newton method. This last technique uses a new proposed approach to predict the phase of the B_1^+ field in a direct fashion.

These techniques provide fast and accurate simulation results for a two-dimensional abdominal body slice placed in a 3T MRI scanner for different pad scenarios. From these results it can be concluded that both proposed techniques generate comparable pads, which are able to increase the homogeneity of the B_1^+ field.

A comparison between the two techniques is made. The Gauss-Newton method provides a fast, robust and accurate optimization technique for large scale problems, but offers less flexibility and insight to the data compared to the method via inspection.

The flexibility of the method via inspection and the insight it provides is shown for different scenarios (pad location, multiple pads, pad shape, pad thickness), where the effect of the optimal permittivity and conductivity on the homogeneity of the resulting B_1^+ field is simulated. Even the maximum allowed SAR can be incorporated in this pad optimization technique.

Preface

This thesis presents the work of 9 months research into optimization techniques for dielectric pads in MRI and it has been written to obtain the degree of Master of Science in Electrical Engineering at Delft University of Technology. The project was supervised by dr.ir. R.F. Remis and is closely related to the Ph.D research work of ir. J.H.F. van Gemert.

In the early stage of my study I developed already an interest in how electrical engineering can be applied in health care. During a CAS group info lunch I became enthusiastic about MRI, an interesting application of electrical engineering in health care. Rob Remis showed me some interesting topics in MRI and pointed me to the course wavefield imaging he taught. During that course I became even more excited about the examples Rob showed us during classes. From that point I knew that I wanted to work on MRI with Rob for my master thesis, so in September I contacted Rob. It turned out that Jeroen had some promising research results which are used as basis for my research.

M. M. J. Gerlach
Delft, July 2016

Acknowledgments

I would like to thank a number of people, because I could never have accomplished this thesis without their help and support.

First of all I want to gratefully thank my supervisor Rob Remis for his support and guidance through the master's thesis project. It was great to work together and to see your commitment and enthusiasm about the results I showed during our weekly meetings. You always made some time for me in your busy schedule to give me some new insights when I got stuck. Your understanding and support during a difficult time in my life was also great. It is absolutely clear to me why my colleague students elected you as best teacher at EEMCS.

I would also like to acknowledge Jeroen for introducing me to MRI and sharing his code (and Duke), and for his help with correcting this thesis.

I would like to express my gratitude to the other members of my committee, prof. dr. ir. A. -J. van der Veen and prof. dr. ir. A. G. Webb for taking the time.

I would also like to thank the other students I shared the CAS master student room with. It was nice to work in the same room and struggle with the same things during the project. Fortunately, I was not the only student working on MRI, so we could have some fruitful discussions on MRI.

Finally, I must express my very profound gratitude to my family and friends for providing me with unfailing support and continuous encouragement throughout my years of study and through the process of researching and writing this thesis. This accomplishment would not have been possible without them. Thank you.

Contents

List of Figures

List of Tables

1

Introduction

1.1. MRI

Magnetic Resonance Imaging (MRI) is widely used for medical diagnosis and laboratory research. Unlike other imaging techniques such as x-ray, MRI does not make use of harmful ionizing radiation. Another advantage is the sensitivity of Magnetic Resonance (MR) to a wide variety of tissue parameters and hence it can provide more information by using different pulse sequences [19]. MRI is able to produce high resolution and high contrast images through the body without any risk, which made it the fastest growing imaging modality in recent years. Extensive research is done to further improve the Signal to Noise Ratio (SNR), resulting in increased image quality or reduction in scanning time for the same image quality. Therefore the field strength is increased over the years which leads to high-field MRI systems [23].

The magnetic field in MRI is created by a strong main magnet provided by a superconducting magnet that creates a uniform static magnetic field directed in the longitudinal direction, the B_0 field oriented by convention in the *z*-direction of a Cartesian reference frame. Nowadays, superconducting magnets of 1.5 T up to even 7 T are commonly used as main magnet. Hydrogen protons are present in a very high density within the human body (the human body contain a lot of water), and since the hydrogen proton has a small magnetic moment it will align to this static field. These protons spin around their axes with the Larmor frequency, which is known as precession [16]. When a secondary circularly polarized Radio Frequency (RF) field is applied at this particular frequency the protons can be flipped in the plane perpendicular to the z-direction, the transverse xy-plane. When the RF-field is released the protons fall back in their former equilibrium position while emitting energy. This energy is picked up and converted into a detailed MR scan.[1]

However, only a specific part of the RF field is able to flip the magnetization out of its equilibrium towards the xy-plane where it can be measured [8]. Such field is called the left-handed circularly polarized RF field, the B_1^+ field. To obtain high-quality images this field needs to be as homogeneous as possible with a sufficient field strength, although the maximum field strength is related to the electric field strength which is bounded by the allowed Specific Absorption Rate (SAR) [27].

The Larmor frequency of the B_1^+ field is linearly related to the static field strength, hence for higher field strengths the resonance frequency increases. At some point, the wavelength of the B_1^+ field becomes comparable to the dimensions of the human body. This causes a major problem in high-field MRI, namely the inhomogeneity of the B_1^+ field due to interference effects [1][5]. An example of this effect is given in Figure 1.1a where signal drop-outs are clearly visible as black spots in the image due to destructive interference. Also the opposite is possible, constructive interference that leads to very bright spots in the image with related so-called hot spots in the electric field, which might exceed the allowed SAR and therefore becomes problematic as well.

[1] For a more thorough but still easy (as the title implies) explanation I suggest reading `http://www.stat.columbia.edu/~martin/Tools/MRI_Made_Easy.pdf`.

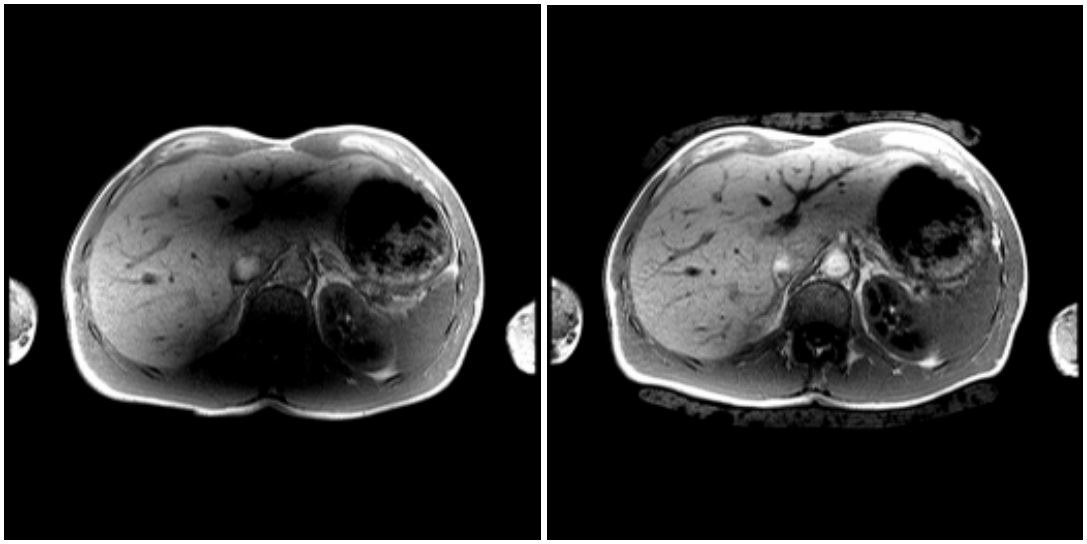

(a) Scan without pad **(b)** Scan with pad

Figure 1.1: Abdominal scans of a patient in a 3T MRI system. (a) clearly shows the signal drop-outs due to the interference effects. These effects are removed in (b) by making use of dielectric material (pads), placed anterior and posterior of the patient.

1.2. RF shimming with dielectric pads

By using shimming techniques the interference problem can be overcome by tailoring the field to compensate for these effects. This can be done via placing and tuning antennas, often referred to as active shimming [28] or by placing dielectric objects close to the region of interest (ROI), called passive shimming [9]. Passive shimming is a more practical solution because no hardware additions to an existing MR system are needed. Dielectrics in the form of high-permittivity pads are used instead, which are relatively cheap and easy to fabricate. The pads induce a secondary magnetic field which is able to overcome the signal drop-outs due to interference effects, only when designed correctly. Figure 1.1b shows the resulting image when pads with carefully selected parameters are placed. These parameters are location of the pad, the material properties (permittivity and conductivity), the shape and the number of pads. Selecting the right parameters is however challenging and also patient specific unfortunately [3]. Therefore, finding the right pad parameters quickly and accurately is of great interest so that the right pads for a patient can be selected immediately, without several hospital visits and multiple scans.

There are several materials and compositions used to fabricate pads, having typically relative permittivity values of 80 up to 1000. Water and aqueous solutions are one of the frequent used materials with a relative permittivity of approximately 60 to 80 [24]. Another possible material for example is calcium titanate with a typical relative permittivity around 150 [14]. Recent research has shown that barium titanate can be used for even higher relative permittivities up to 300 [17], and there are even materials with a permittivity of 800 and 1200 [21], those materials are sealed together in a pad, which is most of the time rectangular shaped. The pad will follow the contour of the subject where it is placed, because of the flexibility of the material. Small compartments in the pad can be used to prevent for spatial variation in the pad itself due to mechanical stress [25], however spatial variation can be a design criteria as well.

1.3. Problem definition

To find the influence of a specific dielectric pad in a specific configuration (human subject, coils, etc.) we need to find the magnetic fields. To this end we solve the Maxwell's equations to obtain the electromagnetic fields. As mentioned before, it is of importance to do this as quickly as possible. However, with the traditional solvers it will take a significant amount of time to calculate the fields for the large amount of possible pad configurations and hence, to select the optimal pad (the pad that results in the most homogeneous B_1^+ field). For example, solving for a pad placed on 5 different possible locations,

with 5 different dimensions and 2 different permittivity values results already in 50 simulations. Alternatively, the problem size can be reduced by dividing the domain into a stationary background domain (the body in the MR-scanner), which can be calculated offline and a field of small dimension which is induced by the pad only [4]. Therefore, the B_1^+ field inside the body can be computed efficiently by making use of *Sherman-Morrison-Woodbury* formula [26], where we have exploited the fact that the pad forms a small perturbation with respect to the background configuration. This is the approach that we will follow in this thesis.

Outline

The approach described above is shown in more detail in Chapter 2. In Chapter 3 the optimal pad parameters are experimentally determined by solving an optimization problem. In Chapter 4 we determine the optimal pad parameters in a more analytical way, in combination with our proposed new method for phase updating. Some conclusions are drawn in chapter 5.

2

An integral equation approach

In this chapter we discuss an integral equation approach that shows that the B_1^+-field inside the human body can be calculated efficiently by noticing that a pad introduces only a low-rank perturbation of the original system. Since we have to deal with electromagnetic fields, a good starting point is obvious Maxwell's equations. With these equations we compute first the electromagnetic fields present in absence of the human body, the background field. Next, the scattered field can be calculated, which let us compute the total transmitted electric field when the human body is present, under the assumption that the contrast is known. We use the *Sherman-Morrison-Woodbury* formula to compute the total transmitted electric field efficiency in a discretized form, which leads us finally to the B_1^+ field in a single step.

2.1. Maxwell's equations

The behaviour of the electromagnetic field is described by Maxwell's time-harmonic field equations

$$-\boldsymbol{\nabla} \times \hat{\mathbf{H}} + \sigma \hat{\mathbf{E}} + \mathrm{j}\omega\epsilon \hat{\mathbf{E}} = -\hat{\mathbf{J}}^{\text{ext}}, \tag{2.1}$$

and

$$\boldsymbol{\nabla} \times \hat{\mathbf{E}} + \mathrm{j}\omega\mu \hat{\mathbf{H}} = \mathbf{0}. \tag{2.2}$$

Equation 2.1 is known as the Maxwell-Ampere equation, where $\hat{\mathbf{H}}$ is the magnetizing field (A/m), $\hat{\mathbf{E}}$ the electric field (V/m), and $\hat{\mathbf{J}}^{\text{ext}}$ is the external electric-current density (A/m^2). Furthermore, Equation 2.2 is also known as Faraday's law. We cannot solve the above equations since only $\hat{\mathbf{J}}^{\text{ext}}$ is known, so the number of unknowns is larger than the number of known quantities. Fortunately, the medium parameters in vacuum are also known where the permeability of vacuum $\mu = \mu_0 = 4\pi \cdot 10^{-7}$ (H/m) and the permittivity $\epsilon = \epsilon_0 = 1/c_0^2\mu_0$ (F/m), with $c_0 = 299792458$ (m/s) the electromagnetic wave speed in vacuum. The conductivity $\sigma = 0$ (S/m) in vacuum.

A background model with a so-called scattering formalism is introduced to find the electromagnetic field in the transmit state of the MRI scanner. Therefore we exploit the linearity of Maxwell's equations and simply add the background and scattered fields to arrive at a explicit integral representations for the total electromagnetic field. The background field ($\hat{\mathbf{H}}_{\text{b;tr}}$ and $\hat{\mathbf{E}}_{\text{b;tr}}$) is defined as the electromagnetic field that would be present if the human body is absent and the scattered field ($\hat{\mathbf{H}}_{\text{sc;tr}}$ and $\hat{\mathbf{E}}_{\text{sc;tr}}$) for which the human body acts as a source. The used configuration is depicted in Figure 2.1, where the external electric-current density $\hat{\mathbf{J}}^{\text{ext}}$ is given by RF antennas that occupies a bounded source domain $\mathbb{D}_{\text{src}}$ in $\mathbb{R}^3$. This generates an electromagnetic field that is incident upon the human body, which occupies the bounded object domain $\mathbb{D}_{\text{obj}}$, when we are not only looking at the background field and is embedded in vacuum for simplicity.

Note that the medium parameters for vacuum hold for both the background field as for the total electromagnetic field ($\hat{\mathbf{H}}_{\text{tr}}$ and $\hat{\mathbf{E}}_{\text{tr}}$) outside the bounded object domain $\mathbb{D}_{\text{obj}}$, since this domain is embedded in vacuum. There is obvious no external electric-current density inside the object domain, so $\hat{\mathbf{J}}^{\text{ext}} = \mathbf{0}$ in that case. Also the medium inside the object domain differ, the conductivity σ in Equation 2.1 exists

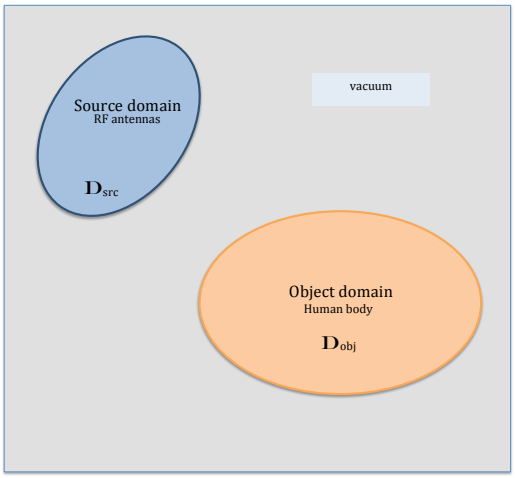

Figure 2.1: The electromagnetic transmit field generated by external sources located in the source domain $\mathbb{D}_{src}$ and if the human body is present the bounded object domain $\mathbb{D}_{obj}$ occupied by the human body, surrounded by vacuum.

and the permittivity $\epsilon = \epsilon_r \epsilon_0$. We assume that the permeability of the medium, given in Equation 2.2 remains the same as the permeability for vacuum, μ_0.

If we subtract the background field equations from the total field equations, we obtain

$$-\boldsymbol{\nabla} \times \hat{\mathbf{H}}_{sc;tr} + j\omega\epsilon_0 \hat{\mathbf{E}}_{sc;tr} = -\hat{\mathbf{J}}_{sc;tr}(\mathbf{r}, \omega) \tag{2.3}$$

and

$$\boldsymbol{\nabla} \times \hat{\mathbf{E}}_{sc;tr} + j\omega\mu_0 \hat{\mathbf{H}}_{sc,tr} = \mathbf{0}, \tag{2.4}$$

with the scattering fields as

$$\hat{\mathbf{H}}_{sc;tr} = \hat{\mathbf{H}}_{tr} - \hat{\mathbf{H}}_{b;tr}, \quad \hat{\mathbf{E}}_{sc;tr} = \hat{\mathbf{E}}_{tr} - \hat{\mathbf{E}}_{b;tr},$$

and the scattering source as

$$\hat{\mathbf{J}}^{sc;tr}(\mathbf{r}, \omega) = \begin{cases} \mathbf{0} & \text{if } \mathbf{r} \notin \mathbb{D}_{obj} \\ \{\sigma(\mathbf{r}) + j\omega[\epsilon(\mathbf{r}) - \epsilon_0]\}\hat{\mathbf{E}}_{tr}(\mathbf{r}, \omega) & \text{if } \mathbf{r} \in \mathbb{D}_{obj}. \end{cases}$$

Now equation 2.3 and equation 2.4 are of the same form as the time-harmonic field equation we had before. The magnetizing field can be eliminated by combining these two equations. This gives

$$\nabla^2 \hat{\mathbf{E}}_{sc;tr} - \gamma^2 \hat{\mathbf{E}}_{sc;tr} = j\omega\mu_0 \hat{\mathbf{J}}^{sc;tr} - (j\omega\epsilon_0)^{-1} \boldsymbol{\nabla}\boldsymbol{\nabla} \cdot \hat{\mathbf{J}}^{sc;tr},$$

where $\gamma = j\omega/c_0$ is the propagation coefficient. We introduce Green's function $\hat{G}$ in order to solve this differential equation

$$\hat{G}(\mathbf{r}, \omega) = \frac{\exp(-\gamma|\mathbf{r}|)}{4\pi|\mathbf{r}|} \quad \text{for } |\mathbf{r}| \neq 0.$$

The solution for the electric field strength of the scattered field can be written by the following integral representation

$$\begin{aligned} \hat{\mathbf{E}}_{sc;tr}(\mathbf{r}, \omega) = &- j\omega\mu_0 \int_{\mathbf{r}' \in \mathbb{D}_{obj}} \hat{G}(\mathbf{r} - \mathbf{r}', \omega) \hat{\mathbf{J}}^{sc;tr}(\mathbf{r}', \omega) dV \\ &+ (j\omega\epsilon_0)^{-1} \boldsymbol{\nabla}\boldsymbol{\nabla} \cdot \int_{\mathbf{r}' \in \mathbb{D}_{obj}} \hat{G}(\mathbf{r} - \mathbf{r}', \omega) \hat{\mathbf{J}}^{sc;tr}(\mathbf{r}', \omega) dV. \end{aligned} \tag{2.5}$$

By using the definition of the scattered field this results in the integral equation

$$\hat{\mathbf{E}}_{\text{tr}}(\mathbf{r},\omega) - \left(\frac{\omega}{c_0}\right)^2 \int_{\mathbf{r}'\in\mathbb{D}_{obj}} \hat{G}(\mathbf{r}-\mathbf{r}',\omega)\hat{\chi}(\mathbf{r}',\omega)\hat{\mathbf{E}}_{\text{tr}}(\mathbf{r}',\omega)dV \\ - \boldsymbol{\nabla}\boldsymbol{\nabla}\cdot\int_{\mathbf{r}'\in\mathbb{D}_{\text{obj}}} \hat{G}(\mathbf{r}-\mathbf{r}',\omega)\hat{\chi}(\mathbf{r}',\omega)\hat{\mathbf{E}}_{\text{tr}}(\mathbf{r}',\omega)dV = \hat{\mathbf{E}}_{\text{b;tr}}(\mathbf{r},\omega), \tag{2.6}$$

with $\mathbf{r}\in\mathbb{D}_{\text{obj}}$ and where we have introduced the contrast function as

$$\hat{\chi}(\mathbf{r},\omega) = \epsilon_r(\mathbf{r}) - 1 - \mathrm{j}\frac{\sigma(\mathbf{r})}{\omega\epsilon_0}. \tag{2.7}$$

We can write this integral equation more compactly by introducing an operator $\mathscr{L}$ which yields

$$\mathcal{L}\hat{\mathbf{E}}_{\text{tr}} = \hat{\mathbf{E}}_{\text{tr}}(\mathbf{r},\omega) - \left(\frac{\omega}{c_0}\right)^2 \int_{\mathbf{r}'\in\mathbb{D}_{\text{obj}}} \hat{G}(\mathbf{r}-\mathbf{r}',\omega)\hat{\chi}(\mathbf{r}',\omega)\hat{\mathbf{E}}_{\text{tr}}(\mathbf{r}',\omega)dV \\ - \boldsymbol{\nabla}\boldsymbol{\nabla}\cdot\int_{\mathbf{r}'\in\mathbb{D}_{\text{obj}}} \hat{G}(\mathbf{r}-\mathbf{r}',\omega)\hat{\chi}(\mathbf{r}',\omega)\hat{\mathbf{E}}_{\text{tr}}(\mathbf{r}',\omega)dV, \tag{2.8}$$

and now write Equation 2.6 as follow

$$\mathcal{L}\hat{\mathbf{E}}_{\text{tr}} = \hat{\mathbf{E}}_{\text{b;tr}} \quad \text{with} \quad \mathbf{r}\in\mathbb{D}_{\text{obj}}. \tag{2.9}$$

2.2. Sherman-Morrison-Woodbury

Furthermore, the continuous integral equation is discretized for the 2D case in Appendix B, resulting in the following equation

$$(\mathbf{I} - \mathbf{G}\mathbf{X}_{\text{body}} - \mathbf{G}\mathbf{X}_{\text{pad}})\tilde{\mathbf{e}}_{\text{tr}} = \mathbf{e}_{\text{b;tr}}, \tag{2.10}$$

where $\tilde{\mathbf{e}}_{\text{tr}}$ contains the total electric field and $\mathbf{e}_{\text{b;tr}}$ is the background electric field. Furthermore, $\mathbf{I}$ is the identity matrix, $\mathbf{X}$ is a diagonal matrix with the contrast function values for the body and pad respectively, and matrix $\mathbf{G}$ is the Green's matrix. This matrix is constructed by making use of a uniform grid to discretize the integral equation, so the product of a vector with this matrix $\mathbf{G}$ can be calculated in a fast way via Fast Fourier Transform (FFT) [12].

By comparing $\mathbf{X}_{\text{body}}$ of size K-by-K and $\mathbf{X}_{\text{pad}}$ of size L-by-L, where L is the number of voxels/pixels occupied by the pad, we notice that L is much smaller than K as already mentioned before. By making use of Sherman-Morrison-Woodbury we can write the total electric field with pads in terms of the total electric field without pads, where the pads introduce a rank L perturbation of the system without any pads. Using matrix algebra we have $\mathbf{G}\mathbf{X}_{\text{pad}} = \mathbf{U}\mathbf{V}^T$ with

$$\mathbf{U} = \mathbf{G}\mathbf{S}$$

and

$$\mathbf{V} = \mathbf{S}\mathbf{X}_{\text{pad}},$$

where $\mathbf{S}$ is a K-by-L support matrix as

$$\mathbf{S} = [\mathbf{e}_{j1}, \mathbf{e}_{j2}, ..., \mathbf{e}_{jP}],$$

with $\mathbf{e}_j$ the jth canonical basis vector. Apply the *Sherman-Morrison-Woodbury formula*, we find

$$\tilde{\mathbf{e}}_{\text{tr}} = \mathbf{e}_{\text{tr}} + \mathbf{Z}(\mathbf{I} - \mathbf{V}^T\mathbf{Z})^{-1}\mathbf{V}^T\mathbf{e}_{\text{tr}}, \quad \text{where} \quad \mathbf{Z} = (\mathbf{I} - \mathbf{G}\mathbf{X}_{\text{body}})^{-1}\mathbf{U}, \tag{2.11}$$

where $\mathbf{e}_{\text{tr}}$ contains the total electric field without pad. Notice that only $\mathbf{V}$ depends on the contrast of the pad, therefore matrix $\mathbf{Z}$ can be calculated offline with a iterative solver, for example GMRES. The inverse $(\mathbf{I}-\mathbf{V}^T\mathbf{Z})^{-1}$ is easily computed, since the number of perturbations L is usually small. Therefore, different pads can be calculated very efficiently with Equation 2.11 by making use of the offline library matrix $\mathbf{Z}$.

2.3. The RF field

The calculation of the left-handed and circularly polarized time-harmonic RF field inside the human body defined as

$$\hat{\mathbf{B}}_1^+ = \hat{B}_1^+(\mathbf{i}_x - \mathrm{j}\mathbf{i}_y) \quad \text{with} \quad \hat{B}_1^+ = \frac{\hat{B}_x + \mathrm{j}\hat{B}_y}{2}, \tag{2.12}$$

is straightforward now by applying Faradays's law, Equation 2.2 for both components separately. From Appendix B we have

$$\frac{\partial}{\partial y}\hat{E}_z + \mathrm{j}\omega\mu\hat{H}_x = 0, \tag{2.13}$$

and

$$-\frac{\partial}{\partial x}\hat{E}_z + \mathrm{j}\omega\mu\hat{H}_y = 0. \tag{2.14}$$

Rewriting this in terms of its magnetic field component by making use of the constitutive relation $\hat{\mathbf{B}} = \mu\hat{\mathbf{H}}$, results in the following equations

$$\mathrm{j}\omega\hat{B}_x = -\frac{\partial}{\partial y}\hat{E}_z, \tag{2.15}$$

and

$$\mathrm{j}\omega\hat{B}_y = \frac{\partial}{\partial x}\hat{E}_z. \tag{2.16}$$

The above expressions are approximated by centered finite-differences to solve them in the discretized domain, where $\mathbf{E}_z$ denotes the M-by-N electric field matrix of values of the discretization cells. Therefore, we introduce the $(M-2)$-by-M differentiation matrix

$$\mathbf{X} = \frac{1}{2\delta x}\begin{pmatrix} -1 & 0 & 1 & & \\ & -1 & 0 & 1 & \\ & & & -1 & 0 & 1 \end{pmatrix}, \tag{2.17}$$

and the $(N-2)$-by-N differentiation matrix

$$\mathbf{Y} = \frac{1}{2\delta y}\begin{pmatrix} -1 & 0 & 1 & & \\ & -1 & 0 & 1 & \\ & & & -1 & 0 & 1 \end{pmatrix}. \tag{2.18}$$

We overcome difficulties in calculating the finite-difference approximation on the boundary of our grid domain by removing the outer boundary cells by introducing the $(M-2)$-by-M restriction matrix

$$\mathbf{R_M} = \begin{pmatrix} 0 & \mathbf{I_M} & 0 \end{pmatrix}, \tag{2.19}$$

where $\mathbf{I_M}$ is the identity matrix of order $M-2$, and the $(N-2)$-by-N restriction matrix

$$\mathbf{R_N} = \begin{pmatrix} 0 & \mathbf{I_N} & 0 \end{pmatrix}, \tag{2.20}$$

where $\mathbf{I_N}$ is the identity matrix of order $N-2$. Finally, with the introduction of all these matrices, we can write the finite-difference approximation of Equation 2.15 and 2.16 as

$$\mathbf{B}_x = \frac{-1}{\mathrm{j}\omega}\mathbf{R}_x\mathbf{E}_z\mathbf{Y}^T, \tag{2.21}$$

and

$$\mathbf{B}_y = \frac{1}{\mathrm{j}\omega}\mathbf{X}\mathbf{E}_z\mathbf{R}_y^T. \tag{2.22}$$

Eventually, we apply the vec-operation to both equations to write these equations in matrix-vector form as

$$\mathbf{b}_x = \frac{-1}{\mathrm{j}\omega}(\mathbf{Y} \otimes \mathbf{R}_x)\,\tilde{\mathbf{e}}_{\mathrm{tr}}, \tag{2.23}$$

and

$$\mathbf{b}_y = \frac{1}{\mathrm{j}\omega} \left(\mathbf{R}_y \otimes \mathbf{X} \right) \tilde{\mathbf{e}}_{\mathrm{tr}}, \tag{2.24}$$

where we used the linearity of the vec-operator and the property [15]

$$\mathrm{vec}\left(\mathbf{A}\mathbf{X}\mathbf{B}^T \right) = \left(\mathbf{B} \otimes \mathbf{A} \right) \mathrm{vec}\left(\mathbf{X} \right), \tag{2.25}$$

where $\otimes$ denotes the Kronecker (tensor) product.

3

Optimal pad design via inspection

In this chapter we will apply the method described in Chapter 2 to calculate the total B_1^+ field for different pad designs. The optimal permittivity and conductivity are determined via inspection where other pad parameters are assumed to be given, for example, the pad location is fixed. These fields are simulated and evaluated in MATLAB.

The simulation configuration is described in Section 3.1. In Section 3.2 two different methods for measuring the homogeneity of the B_1^+ are given. These two methods are tested by simulation for a single fixed pad in Section 3.3, where also the influence of the permittivity and conductivity values of this pad on the SAR are simulated. In Section 3.4 the influence of the position of the pad on the homogeneity of the B_1^+ is tested and in Section 3.5 the simulation results for multiple pads are given. In Section 3.6 the influence of different pad shapes on the homogeneity of B_1^+ is simulated. Finally, the effect of the pad thickness on the optimal permittivity and conductivity is simulated in Section 3.7.

3.1. Simulation configuration

We make use of a male body model called Duke, member of the virtual family provided by IT'IS foundation [6]. This model is placed in a birdcage coil driven by 16 line sources that operates at a frequency of 128 MHz, corresponding to the frequency of a 3T MRI-system. For simplicity, we restrict ourselves to two-dimensional models by taking a transverse slice through the abdominal region of the body and place this slice at the midplane of the birdcage coil. This approach is justified, since the electromagnetic field essentially has a two-dimensional E-polarized field structure at the transverse midplane of a birdcage antenna.

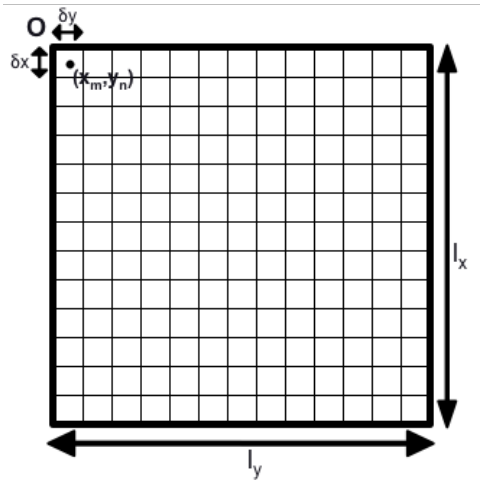

Figure 3.1: The uniform grid used for the discretization, where the number of grid cells (MN) with middle point (x_m, y_n) can vary depending on the size of the grid and the size of each grid cell.

For comparison we compute the electric field strength on both a 4 mm and an 1 mm uniform grid within the slice at the scatter domain with an area of respectively 40 cm-by-40 cm and 33 cm-by-33 cm, defined by the side length l_x and l_y. The region where a pad can be placed is the joint region around the body. For the 4 mm grid we take 7 layers (thickness of the pad is up to 28 mm) and for the 1 mm grid we take 25 possible layers around the body (thickness up to 25 mm). The grid is illustrated in Figure 3.1, where for every voxel/pixel the midpoint x_m is calculated with respect to the origin as follows

$$x_m = \frac{1}{2}\delta x + (m-1)\delta x \quad \text{for} \quad m = 1, 2, \dots, M,$$

with $\delta x = l_x/M$, where the total number of points in the x-direction, denoted by M is 330 for the 1 mm grid ($\delta x = 0.001$ m) and 99 for the 4 mm grid ($\delta x = 0.004$ m). Since the grid is square, we have the same number of points and steps in the y-direction

$$y_n = \frac{1}{2}\delta y + (n-1)\delta y \quad \text{for} \quad n = 1, 2, \dots, N,$$

with $\delta y = l_y/N$. The scattering domain is divided into MN non overlapping discretization cells

$$S_{ij} = \left\{ i\delta x < x < (i+1)\delta x \quad , \quad j\delta y < y < (j+1)\delta y \right\}$$

for $i = 1, 2, \dots, M$ and $j = 1, 2, \dots, N$.

The increase in resolution for the 1 mm grid compared to the 4 mm grid is clearly visible in Figure 3.2, where the contrast of a transverse slice through the abdominal region of Duke is plotted for both cases. However, the differences between the resulting fields are very small as shown in Figure 3.3.

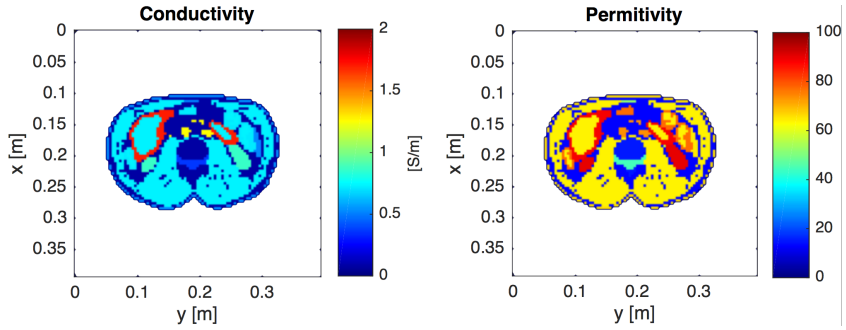

(a) Resolution of 4 mm

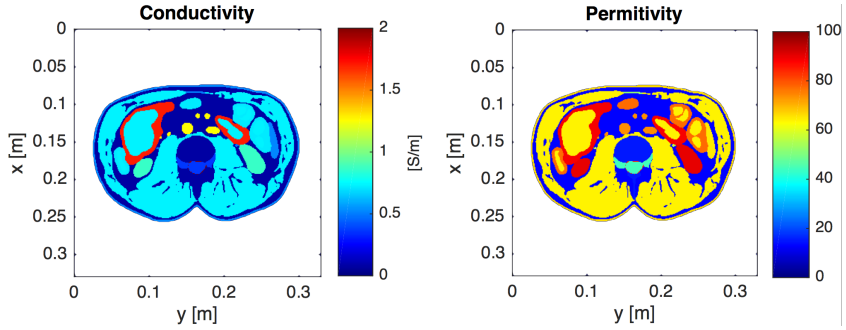

(b) Resolution of 1 mm

Figure 3.2: The contrast of slice 550 of Duke's torso model. The conductivity (left) and permittivity (right) are plotted for 4 mm in (a) and 1 mm in (b).

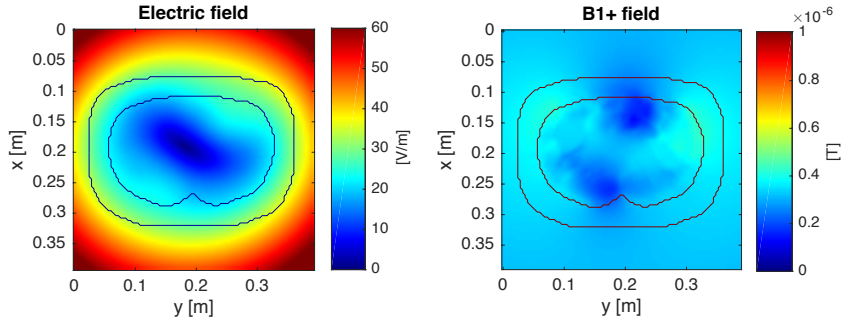

(a) Resolution of 4 mm

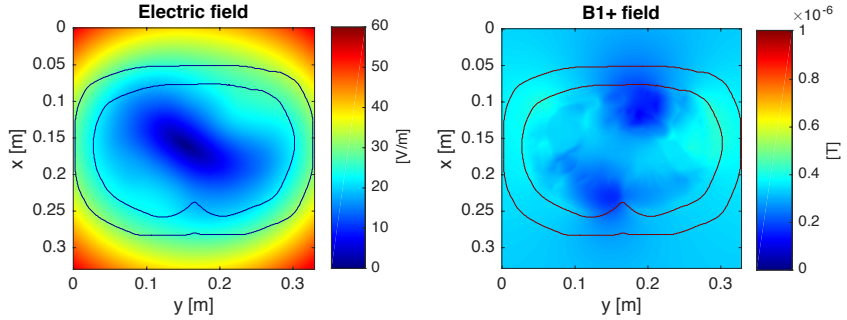

(b) Resolution of 1 mm

Figure 3.3: The z-component of the resulting total electric field (left) and B_1^+ field (right) for 4 mm resolution in (a) and 1 mm resolution in (b). The solid contour lines mark the region where a pad can be placed in between.

3.2. Pad optimization methods via inspection

In section 2.2 we have reduced the computational domain to that of the pad. Therefore the effect of a pad can be found relatively quickly. In this section we fix the pad domain and vary the conductivity and permittivity of the pad for a wide range of values and evaluate the resulting magnetic field. By selecting the best field (the field with the least inhomogeneities) we find the corresponding optimal permittivity and conductivity. Different methods can be used to measure the homogeneity of the total B_1^+ field, hence the minimum value can be easily determined by plotting the functional and observe where the minimum is reached or by just calculating the minimum value itself. One commonly used method to describe the field homogeneity is by looking at the coefficient of variation (CV) [9]. This is done in subsection 3.2.1. A different method is by describing a desired B_1^+ field and measure the error compared to the resulting B_1^+ fields, as done in subsection 3.2.2. Subsequently, in subsection 3.3.3 we determine the optimal pad parameters based on the electric field instead of the B_1^+ field by using the resulting SAR-values. This method is introduced in section 3.3, since it is only used once.

3.2.1. Coefficient of Variation Method

The CV describes the degree of variation in the data by making use of the ratio of standard deviation (SD) to mean (M)

$$CV(\epsilon_r, \sigma) = 100 \frac{SD(|\mathbf{B_1^+}^{\text{inside}}(\epsilon_r, \sigma)|)}{M(|\mathbf{B_1^+}^{\text{inside}}(\epsilon_r, \sigma)|)}, \tag{3.1}$$

since we want to measure 'how homogeneous the resulting field is' we can use the CV for this purpose. Therefore, we determine the total electric field and the corresponding B_1^+ field for different pad values. For each B_1^+ field the CV can be calculated by making use of Equation 3.1. Hence we are only interested in the field inside the body, we only have to calculate the CV for the field inside and we ignore possible variations outside the ROI. The pad that results in the B_1^+ field with the lowest CV value for the B_1^+ field inside is the so called optimal pad, with an optimal permittivity ϵ_r^* and an optimal conductivity σ^*.

3.2.2. Target Field Method

Instead of calculating the variation of the field itself we can describe a desired field and use this field as a target field. For all different pad parameters we again determine the total electric fields and the corresponding B_1^+ fields and subtract the target field from the B_1^+ field which results in an error field

$$\mathbf{err_B}(x_m, y_n, \epsilon_r, \sigma) = \frac{1}{NM} \frac{|\mathbf{B_1^+}(x_m, y_n, \epsilon_r, \sigma)| - |\mathbf{B_1^+}^{\text{desired}}(x_m, y_n)|}{|\mathbf{B_1^+}^{\text{desired}}(x_m, y_n)|} \tag{3.2}$$

for $m = 1, 2, \dots, M$ and $n = 1, 2, \dots, N$. Only the magnitude of the magnetic field is used, since we are only interested in a homogeneous B_1^+ field in its magnitude. From the error field we can now calculate the total error by taking the vector norm as follows

$$err_B(\epsilon_r, \sigma) = \left\| \text{vec}\left(\mathbf{err_B}(x_m, y_n, \epsilon_r, \sigma)\right) \right\|_p, \tag{3.3}$$

for $m = 1, 2, \dots, M$ and $n = 1, 2, \dots, N$, where different p-norms can be used. The pad that results in the smallest err_B is the optimal pad, with an optimal permittivity ϵ_r^* and an optimal conductivity σ^*.

Challenging in this approach is describing a good desired B_1^+ field, which will leads to good pad design. As mentioned before, good imaging quality requires a B_1^+ field that is homogeneous in magnitude. Therefore, the desired B_1^+ field is a homogeneous field inside the ROI created by calculating the mean value for the magnitude of the magnetic field without pad inside the subject area and replacing those values by this mean value. Figure 3.4 shows the magnetic field where no pad is present and the created homogeneous target field based on the field without any pad present.

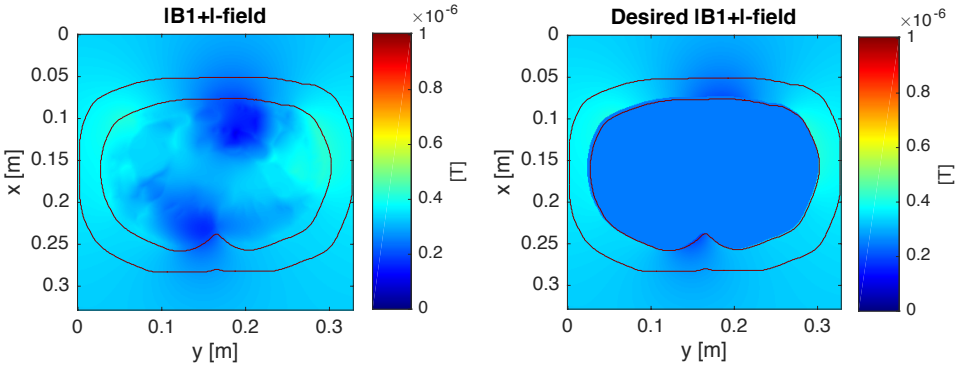

Figure 3.4: The magnitude of the B_1^+ field in case no pad is present and the desired B_1^+ field respectively.

Alternatively, we can prescribe the magnetic field in the ROI instead of describing the whole desired B_1^+ field, since we are not interested in the field outside the subject. Furthermore, we can even reduce the size of the target field by looking at the region of influence of the pad and only use this region, so Equation 3.2 becomes

$$\mathbf{err_B}^{\text{part}}(x_m, y_n, \epsilon_r, \sigma) = \frac{1}{N^{\text{part}}} \frac{|\mathbf{B_1^+}^{\text{part}}(x_m, y_n, \epsilon_r, \sigma)| - |\mathbf{B_1^+}^{\text{desired;part}}(x_m, y_n)|}{|\mathbf{B_1^+}^{\text{desired;part}}(x_m, y_n)|}, \tag{3.4}$$

for all x_m and y_n elements of the ROI and where N^{part} denotes the total number op points inside the ROI.

3.3. Results of single pad optimization

We fix the location and dimension of the pad, by placing one 4 mm thick rectangular pad with a length of 124 mm on the anterior of the abdomen as shown in Figure 3.5. Hence, the permittivity and conductivity are the only free parameters so the total electric field and its corresponding B_1^+ field can be determined easily for different permittivity and conductivity values. This is done for a relative permittivity of 1 to 1000 with steps of 20 and a conductivity in the range from 0 S/m to 5 S/m with steps of 0.05 S/m on both a 4 mm and 1 mm grid.

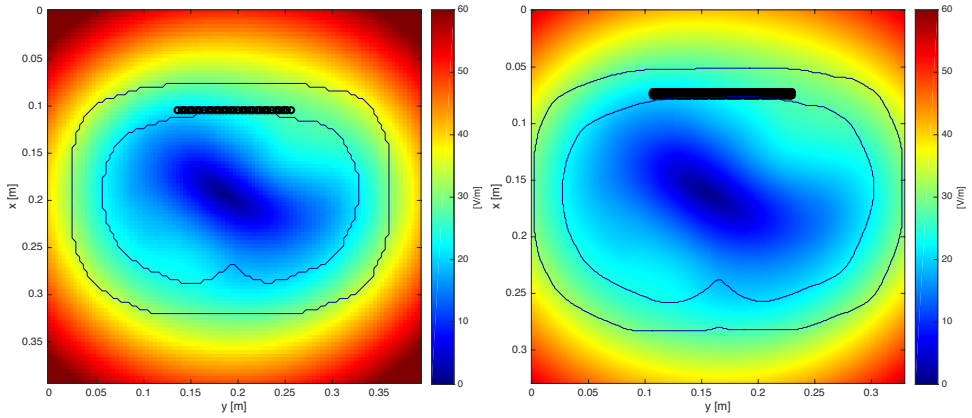

(a) 4 mm resolution **(b)** 1 mm resolution

Figure 3.5: The electric field where black circles are plotted on the grid point occupied by the same pad for both 4 mm and 1 mm grid respectively.

3.3.1. CV method for optimal pad selection

In Table 3.1 the results for the optimal permittivity and conductivity are given. We notice that the results for the CV method on the 4 mm grid are very similar to the results on the 1 mm grid as we expected from the resulting fields in Figure 3.3, which are almost identical as we have mentioned before. The CV for all possible permittivity and conductivity values are made visible in a so called permittivity-conductivity plot as shown in Figure 3.6. From this plot the similarity between the 4 mm and 1 mm grid can also be seen.

	4 mm			1 mm	
ϵ_r^*	σ^* [S/m]	$CV(\epsilon_r^*, \sigma^*)$	ϵ_r^*	σ^* [S/m]	$CV(\epsilon_r^*, \sigma^*)$
540	2.55	14.914%	580	2.60	15.0178%

Table 3.1: CV results for 4 mm and 1 mm resolution, where the CV value is without pad present 19.5073% and 20.1509% respectively.

Furthermore, we can see that the homogeneity of the resulting magnetic field depends mostly on the permittivity, the conductivity is almost invariant to the optimal CV. Figure 3.7 shows the resulting fields for the optimal permittivity and conductivity for both 4 mm and 1 mm. The resulting B_1^+ fields are similar, since the optimal pad parameters are almost the same. When we compare these fields with the field without a pad in Figure 3.3 we clearly see that the field becomes more smooth at the anterior region of the abdomen, the pad makes the field more homogeneous in this region, while the field outside the object become less homogeneous. This corresponds with the CV values (measured inside the object) for the optimal pad, which decreases from 19.5073% to 14.914% for the 4 mm grid and from 20.1509% to 15.0178% for the 1 mm grid.

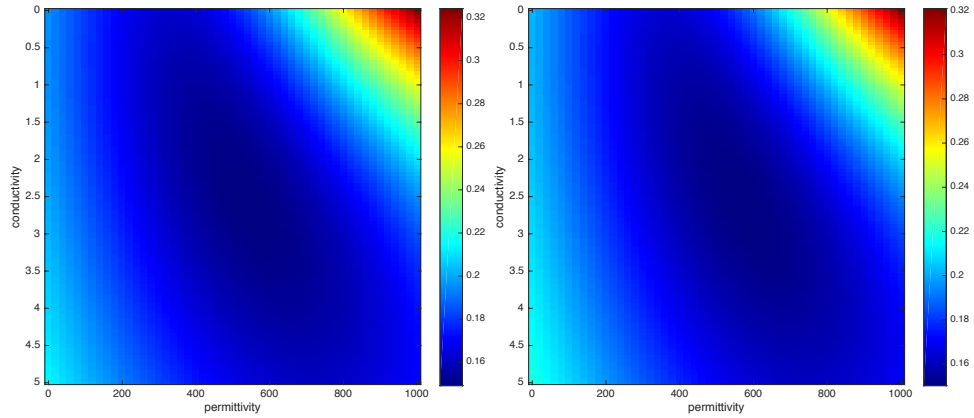

(a) 4 mm grid resolution **(b)** 1 mm grid resolution

Figure 3.6: Permittivity-conductivity plot for the coefficient of variance method.

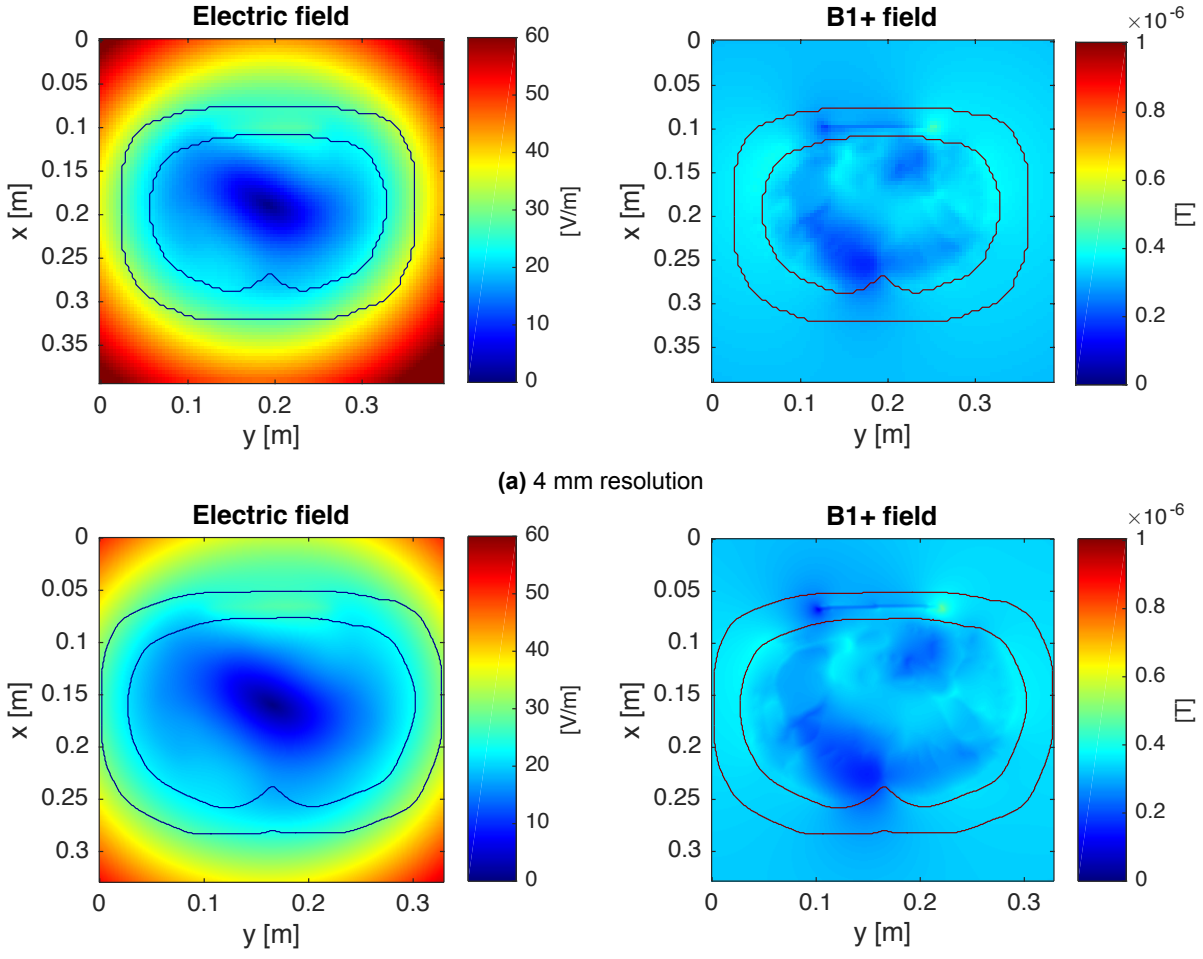

(a) 4 mm resolution

(b) 1 mm resolution

Figure 3.7: The resulting E and B_1^+ field respectively for $CV(\epsilon_r^*, \sigma)$.

3.3.2. Target field method for optimal pad selection

Known field

To test our method in a secure way, we set the permittivity to 200 and the conductivity to 0.2 S/m of the fixed pad described above. The B_1^+ field corresponding to these parameters (the known field) is used in our approach as the desired field. This means our approach should recover the parameters exactly. This is tested first and we also test the robustness of this method by adding white Gaussian noise to the electric field. Hence, disturbance is added to the resulting magnetic field.

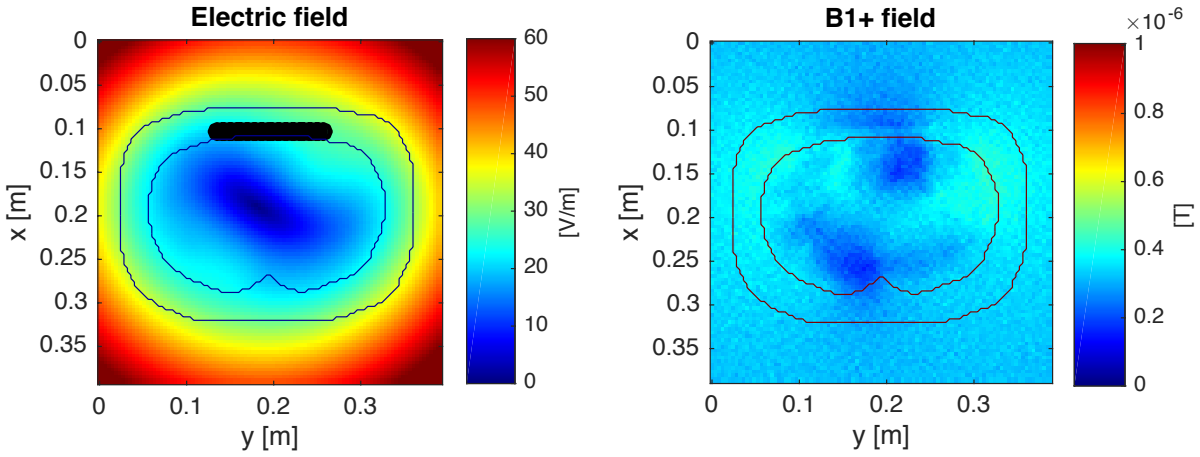

Figure 3.8: The E field with additive white Gaussian noise (SNR of 20 dB) and the resulting B_1^+ field respectively for a pad placed (black line) with σ = 0.2 S/m, ϵ_r=200.

The permittivity and conductivity can be perfectly found for the known field, as expected. Even the original permittivity and conductivity can be almost fully recovered for different norms for an electric field with an SNR of 20 dB due to additive white Gaussian noise, as shown in Table 3.2. Instead of only looking at the magnitude of the magnetic field, we also take a look at the total field since the target field is known and so is the phase. From the results we see that the phase introduces a larger error, while the results do not improve significantly.

	$\lvert B_1^+ \rvert$			B_1^+		
	ϵ_r^*	σ^*[S/m]	$err_B(\epsilon_r^*, \sigma^*)$	ϵ_r^*	$\sigma^{optimal}$[S/m]	$err_B(\epsilon_r^*, \sigma^*)$
p=1	200	0.25	3.4875	200	0.20	5.3571
p=2	180	0.05	0.7614	180	0.25	1.0363
p=∞	220	0.15	3.4230	200	0.35	4.8275

Table 3.2: Results for a known target field with noise created by a pad with ϵ_r=200 and σ = 0.2 S/m. The results are given for the magnitude of the B_1^+ field and the full complex field respectively.

Desired field

The error will increase when using the desired field instead of a known field created with a pad as we did above, since this field can never be fully reached with a single fixed pad. This desired field contains only magnitude data as described in section 3.2.2, since we are only looking for a homogeneous magnitude of the B_1^+ field. The phase does not play an important role in finding the optimal pad and is hard to use due to phase shifts and incorrect measurements [4]. Therefore, only the absolute value of the B_1^+ field is used, as already defined in Equation 3.2.

In table 3.3 the results are given for respectively the 4 mm and 1 mm grid, where different norms are used. We normalized the error for the 1-norm and 2-norm by dividing the error by the total number of points, in order to compare the error between the different grids. For the infinity norm this is not needed, since the infinity norm gives a single value, the maximum. For now we have looked at the field inside the subject only, like we did for the CV method. We notice that the results for the 2-norm are similar to the CV method, hence, the resulting field will be very similar as well. Also, the permittivity-conductivity

plots for the different norms are similar for the 1-norm and 2-norm as can be seen in Figure 3.9, which corresponds with the similar optimal permittivity and conductivity for these norms. Optimizing for the maximum difference between the desired field and the simulated field by using the infinity norm results in much lower optimal permittivity values and also by looking at the permittivity-conductivity plot we can see a much wider valley of values close to the optimal parameters for the infinity norm.

	4 mm grid			1 mm grid		
	ϵ_r^*	σ^*[S/m]	$err_B(\epsilon_r^*, \sigma^*)$	ϵ_r^*	σ^*[S/m]	$err_B(\epsilon_r^*, \sigma^*)$
p=1	620	3.25	0.1148	660	3.35	0.1159
p=2	560	2.85	0.0029	600	2.95	$7.2684\ 10^{-4}$
p=∞	220	2.75	0.4625	300	2.75	0.4730

Table 3.3: Optimal pad parameters for the target field method on both the 4 mm and 1 mm grid.

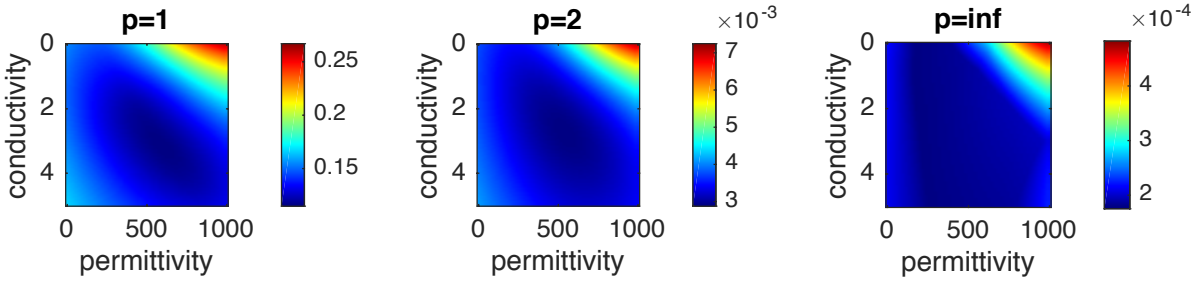

Figure 3.9: Permittivity-conductivity plot for target field method for the 1-norm, 2-norm and infinity norm respectively.

We see again very similar results for a 4 mm and 1 mm grid. Therefore, we choose to do most of the following simulations at the 4 mm grid only for computational time reasons. In order to give an indication of the simulation time we measure the time by running the 2-norm target field simulation in Matlab for the 2 different grid resolutions. The 4 mm grid (the pad occupies 31 cells out of a total of 9801 discretization cells) took 14.4 seconds to run, while the 1 mm grid (the pad occupies 496 discretization cells out of a total of 108900) took 1378.1 seconds to run. All the computation times are measured on a Windows 7 64-bit computer with an Intel Core i5-4690 CPU @ 3.50 GHz and 8 GB of RAM.

As a general remark, note that the use of Matlab's save (v-7.3) function used to read and write columns of the library matrix $\mathbf{Z}$ is much slower than using high-level HDF5 functions. Using a HDF5 dataset with no compression and the chunk size equal to one column of $\mathbf{Z}$ improve the read/write speed with a factor 10. Unfortunately, complex numbers are not supported for a HDF5 dataset, hence by splitting $\mathbf{Z}$ in its real and imaginary part we can still improve read/write speed with a factor 5.

Partial desired field

From the resulting B_1^+ fields in Figure 3.7 we have noticed that a pad placed on a patient affects only the region close to the pad. Therefore, we do not need to prescribe the total desired field inside the subject, instead we can prescribe only the region of the field the pad influences. On the other hand, we can restrict the influence of a pad on the field outside the human body by using the total field as a desired field.

The region a pad influences can be determined by calculating the field induced by a chosen pad only as shown in Figure 3.10 and set a threshold on the field strength. This approach is shown in Figure 3.11 where 3 different thresholds are set with accordingly 3 different regions. The results for these regions and for the field inside the subject and the total field are given in Table 3.4, where the target field error is calculated with the 2-norm. From these results we can see that a partial field gives the same results as a desired field that describes the entire field inside the body, as long as the area of the field does not become smaller than the region the pad influences. The optimal pad parameters for the total field are limited due to negative field effects outside the ROI.

From Figure 3.12 we can see that the magnitude of the resulting B_1^+ fields for the different optimal pad parameters are very similar since the optimal pad parameters are also very similar for the different

target fields. All fields are improved compared to the field without pad, but for the small partial field we see a drop in signal due to the high conductivity and for the total field we see less improvement due to the lower optimal permittivity value.

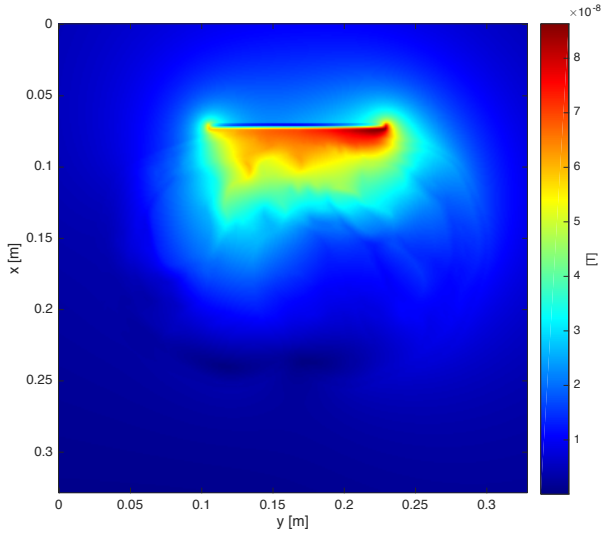

Figure 3.10: The magnitude of the B_1^+ field induced by the pad only.

	ϵ_r^*	σ^*[S/m]	$err_B(\epsilon_r^*, \sigma^*)$
Partial field	660	3.60	8.0794 10^{-4}
Small partial field	540	5.40	0.0018
Large partial field	620	2.95	7.7739 10^{-4}
Inside field	600	2.95	7.2684 10^{-4}
Total field	360	1.55	7.3465 10^{-4}

Table 3.4: Optimal pad parameters for different regions of the field, where the error is calculated by the target field method with the 2 norm.

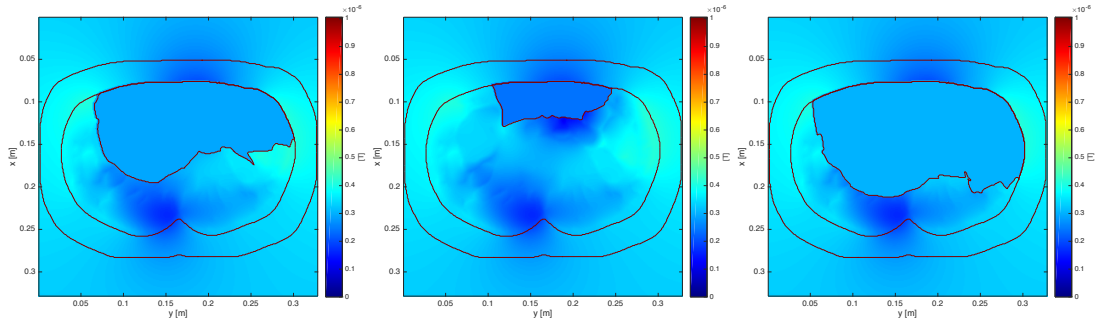

(a) Partial field **(b)** Smal partial field **(c)** Large partial field

Figure 3.11: The selected regions based on the region a pad influences for 3 different thresholds sets.

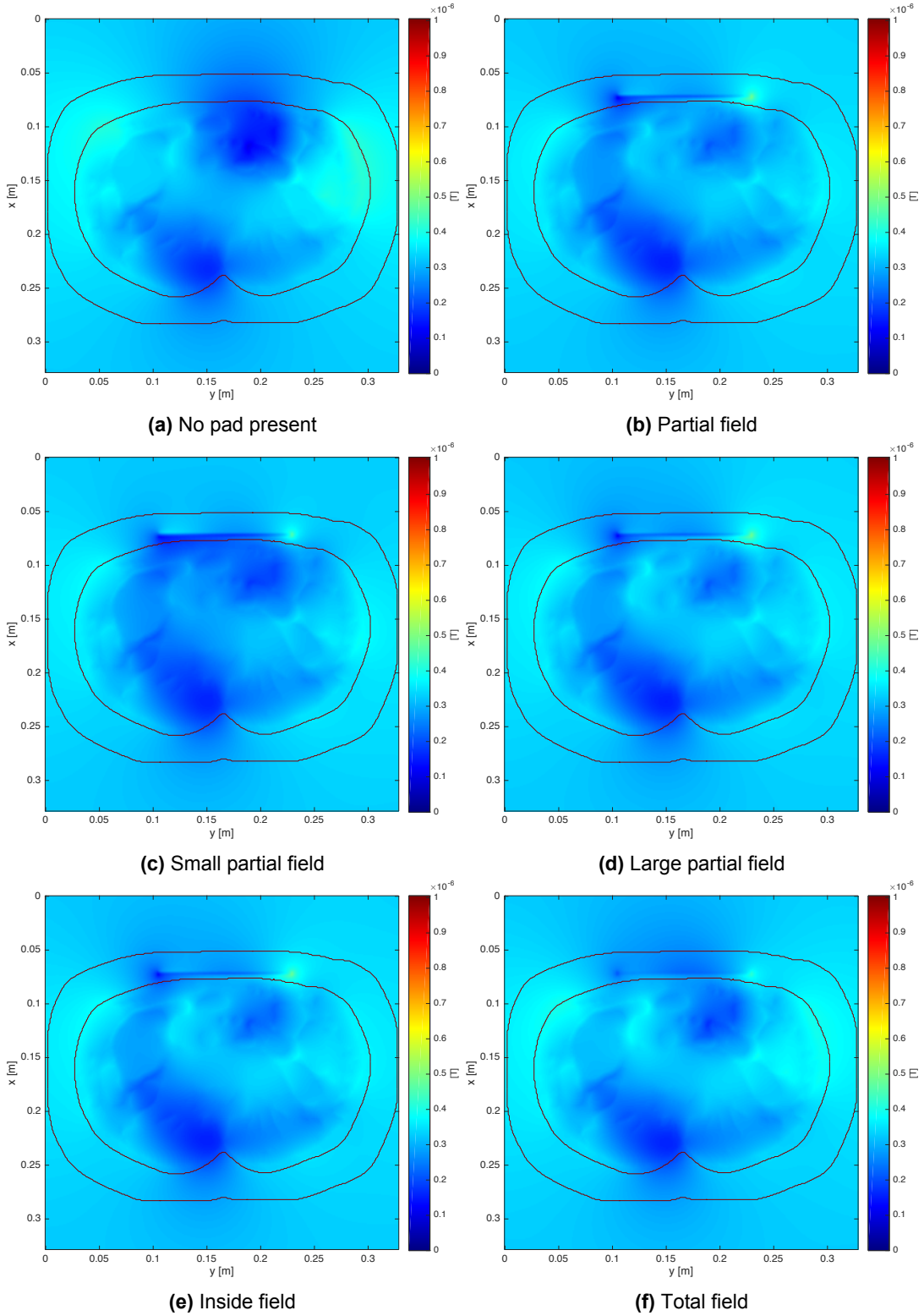

(a) No pad present

(b) Partial field

(c) Small partial field

(d) Large partial field

(e) Inside field

(f) Total field

Figure 3.12: The resulting B_1^+ field in case no pad is present (a) and for the different optimal pad parameters from table 3.4 (b-f).

3.3.3. SAR

SAR is an important safety measure in MRI [7], therefore it is of interest to look for the SAR values for different pad parameters and optimize these parameters according to minimum SAR value inside the patient. This is done by minimizing the following equation

$$err_{\text{SAR}}(\epsilon_r, \sigma) = \sup_{x_m, y_n \in \mathbb{D}_{\text{body}}} \left(\frac{1}{2} \sigma(x_m, y_n) \left| \tilde{\mathbf{E}}_{\text{tr}}(x_m, y_m, \epsilon_r, \sigma) \right|^2 \right). \tag{3.5}$$

From the equation it is easy to see that this method acts on the electric field instead of the magnetic field. Therefore, the calculation of the B_1^+ field from the electric field for every possible pad parameter is not required.

Using only the SAR as an error measure is not desirable, since optimizing for this error result in a decrease in the signal of the electric field due to the quadratic term in equation 3.5. Hence, it results in very high optimal permittivity and conductivity values, so the pad become a shield for the electric field as can be seen in the permittivity-conductivity plot as shown in Figure 3.13 and for the resulting fields in Figure 3.14 where the drop in field strength for the electric field at the location close to the pad is clearly visible. However, the maximum allowed SAR value can be used as secondary optimization criteria in order to prevent hot spots in the resulting electric field. In Figure 3.15 the SAR values for three different configurations are shown.

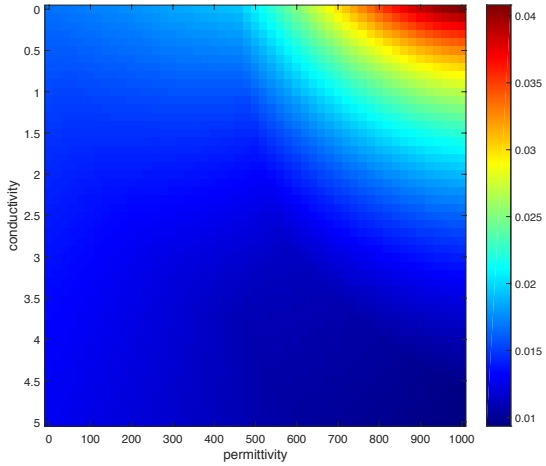

Figure 3.13: Permittivity-conductivity plot for $err_{\text{SAR}}(\epsilon_r, \sigma)$.

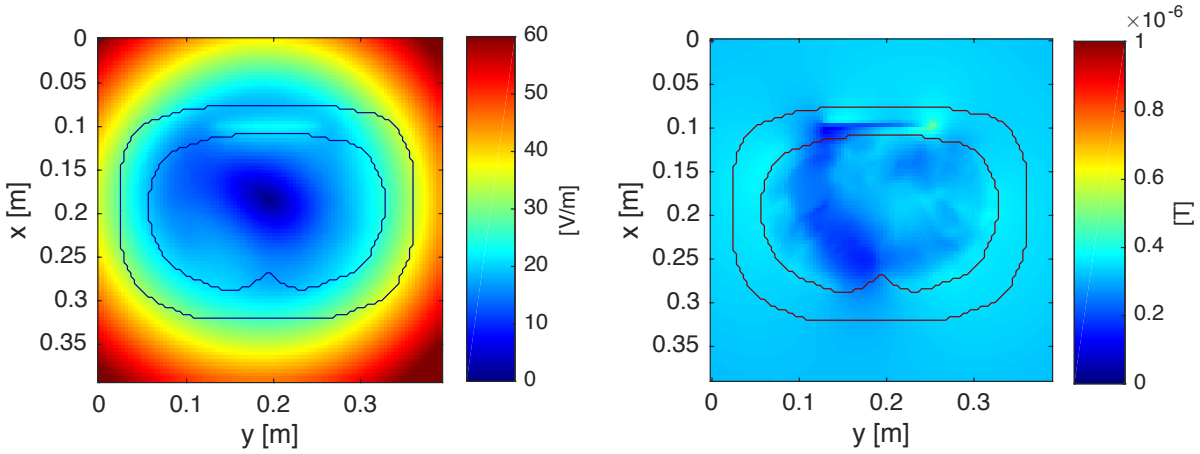

Figure 3.14: The resulting electric and magnetic field respectively for a pad with a high relative permittivity (1000) and conductivity (5 S/m) on a 4 mm grid.

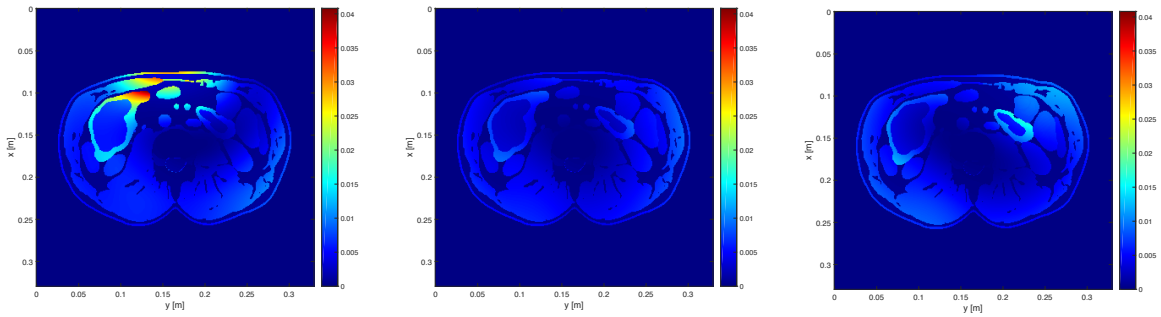

(a) $\epsilon_r^{\text{pad}} = 1000, \sigma^{\text{pad}} = 0$ **(b)** $\epsilon_r^{\text{pad}} = 1000, \sigma^{\text{pad}} = 5$ **(c)** No pad present

Figure 3.15: The SAR inside the body in (a) for a pad with high permittivity and no conductivity, in (b) for a pad with high permittivity and high conductivity, and in (c) when no pad is present.

No need to calculate the B_1^+ field speeds up the optimization procedures a little bit, therefore, we start asking ourselves if we cannot describe a desired electrical field and use this instead of the desired B_1^+ field. Also, this will make it more easy to incorporate the SAR value as a criteria in our approach of selecting the optimal pad. By comparing the electric field of Figure 3.3 with Figure 3.7, we can see the effect a pad has on the E field. In Figure 3.16 we make this effect more clear by plotting the total E field without a pad placed and with 2 pads placed, in order to modify the shape of the E field, such that it will result in a more homogeneous B_1^+ field. In Section 2.3 we have seen that the B_1^+ field is calculated by taking centered finite-differences of the total electric field in the x and y-direction, therefore, it is clear that a more constant change in both directions leads to a more homogeneous B_1^+ field. This can also be visualized by looking at the contour levels for the 2 different total electric fields and compare this with the incident field (which results in a homogeneous B_1^+ field), as can be seen from Figure 3.17. Unfortunately, we came to the conclusion that describing a desired E field is done by prescribing constant centered finite-differences, which is the same as calculating the B_1^+ field and prescribe a homogeneous desired B_1^+ field. Hence, using the E field does not simplify or speed up our pad selecting procedure.

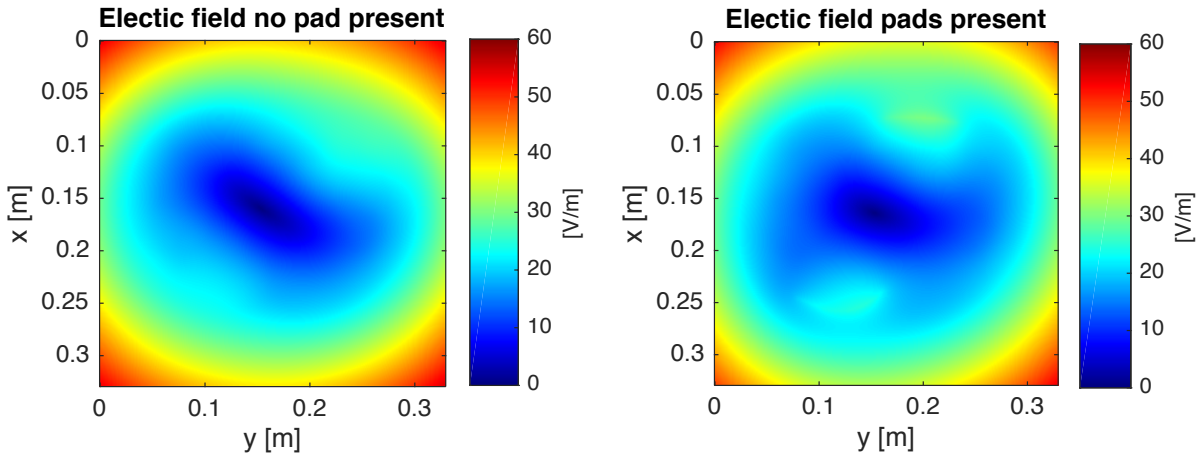

Figure 3.16: The total electric field with no pad present and the total electric field when 2 pads are placed respectively.

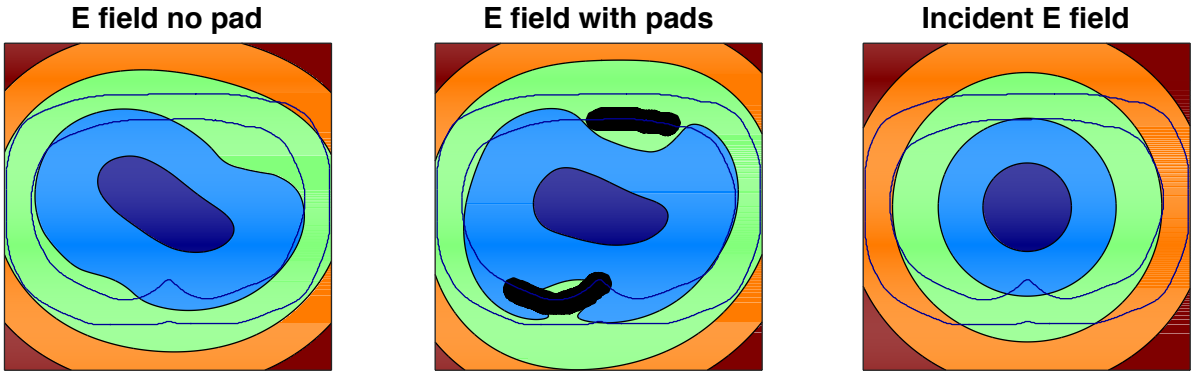

Figure 3.17: The contour levels for the total electric field with no pad present (left), the total electric field with 2 pads present (middle) and the electric incident field (right).

3.4. Influence of pad location on the optimal field

In this section we look furthermore at the effect of the location on the optimal permittivity and conductivity of the pad, and hence on the homogeneity of the resulting B_1^+ field. Figure 3.18 shows possible locations A,B,C and D where a pad can be placed. For each location we will determine the optimal pad parameters for an 1 layer pad with a grid resolution of 4 mm. We can see from the results for the different pad locations given in Table 3.5 that only pads close to inhomogeneities, like dark spots in the B_1^+ field, are able to reduce the error and make the field more homogeneous. This is in line with the small region a pad has influence on, as mentioned before and is also clearly visible at the permittivity-conductivity plots for the different pad locations as shown in Figure 3.19 and for the resulting fields in Figure 3.20, where we can see that the B_1^+ field is improved for pad locations A and C. Location A has the smallest error, hence, location A is the best location to place a pad. On the other hand, we can see from the results that it makes no sense to place a pad on locations B and D.

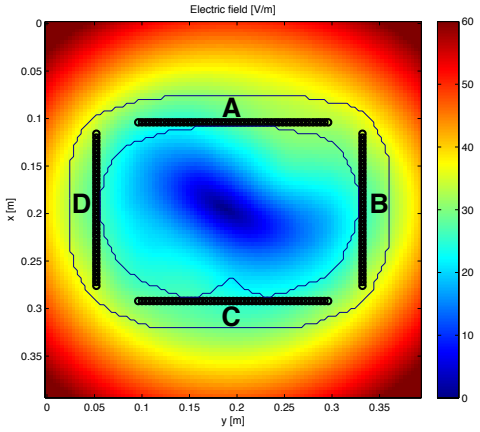

Figure 3.18: Location A, B, C and D are possible locations where a pad can be placed.

	ϵ_r^*	σ^* [S/m]	$err_B(\epsilon_r^*, \sigma^*)$	ϵ_r^*	σ^*[S/m]	$CV(\epsilon_r^*, \sigma^*)$
Location A	460	2.60	0.0030	480	2.9	15.6496%
Location B	0	1.30	0.0037	0	1.15	19.3697%
Location C	400	1.85	0.0034	300	0.7	17.4374%
Location D	0	1.15	0.0037	0	0.40	19.4870%

Table 3.5: The optimal permittivity and conductivity for pads on different locations, CV is 19.5073% in case no pad present.

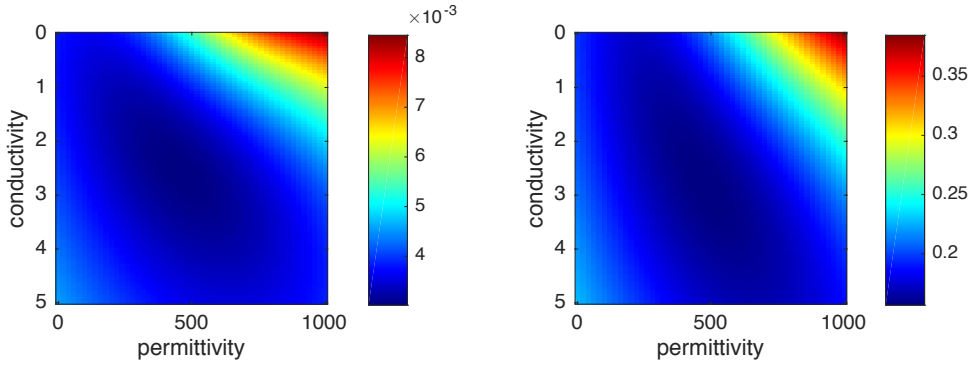

(a) Pad location A

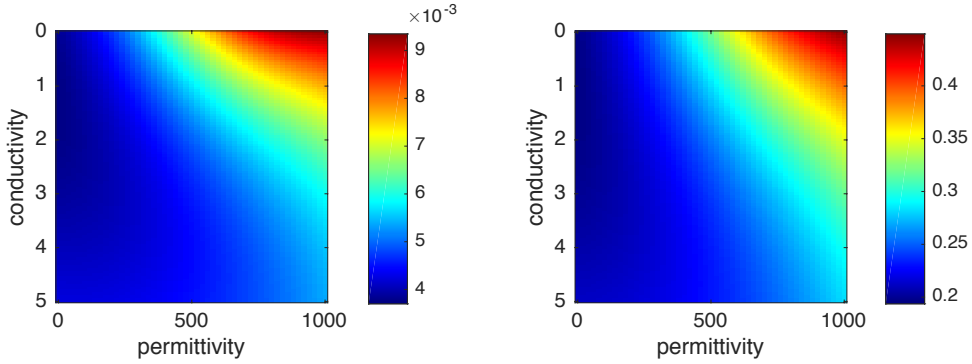

(b) Pad location B

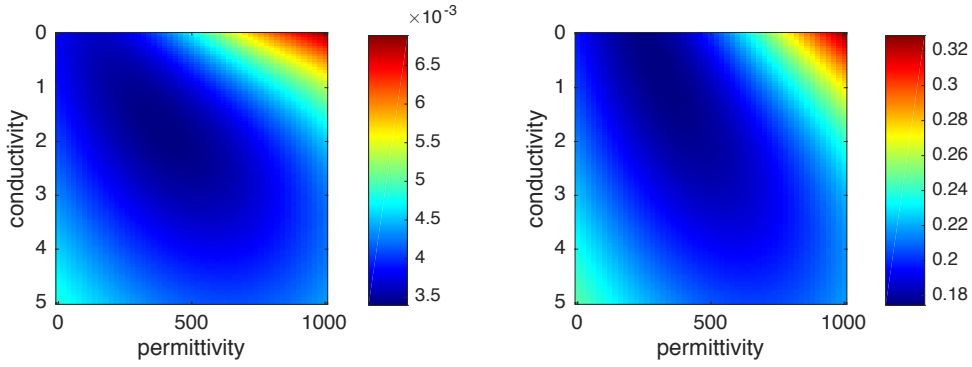

(c) Pad location C

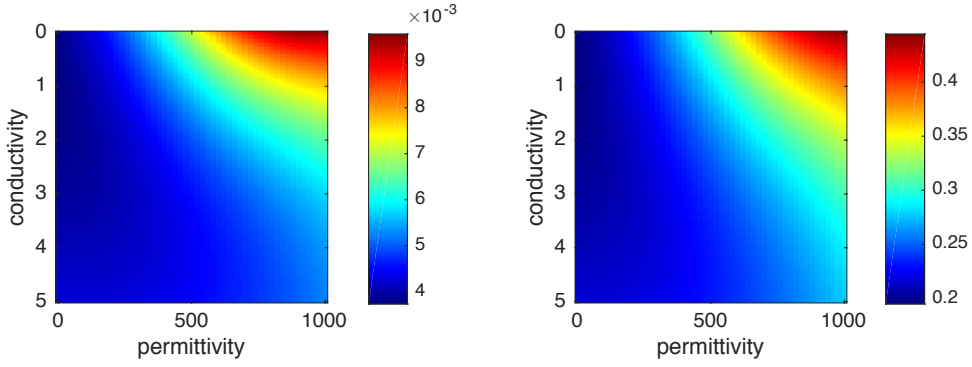

(d) Pad location D

Figure 3.19: Permittivity-conductivity plot for the different locations for both the TF method (left) and the CV method (right).

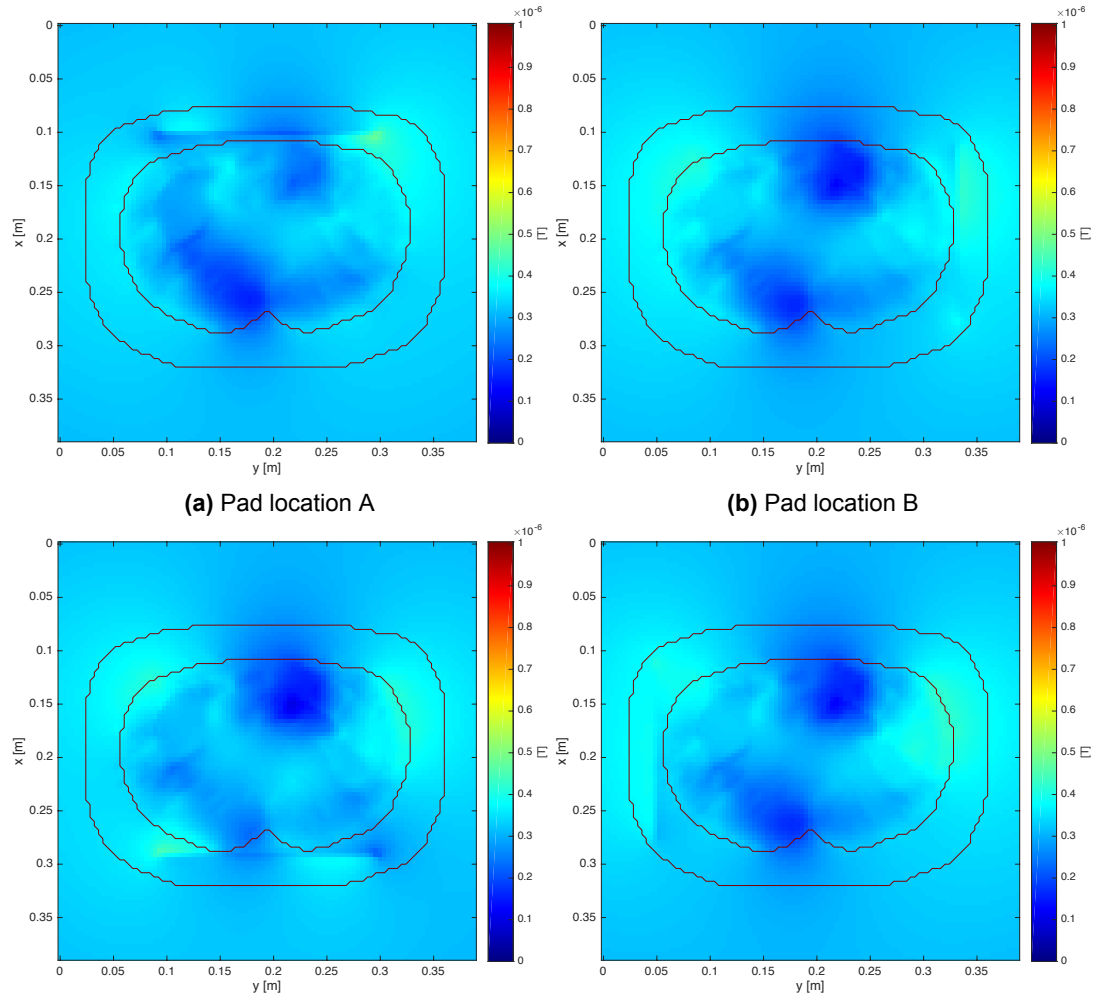

(a) Pad location A

(b) Pad location B

(c) Pad location C

(d) Pad location D

Figure 3.20: The resulting B_1^+ field for the different pad positions with the optimal pad parameters from table 3.4, based on the target field method.

3.5. The usage of multiple pads

From previous results we have already seen that pads influence only small regions of the field and this can also be seen from Figure 3.21, where we subtracted the B_1^+ field with a pad from the B_1^+ field without a pad, in order to show the region a pad influences. Consequently, there will be almost no influence between pads placed far apart. So using multiple pads far apart can be useful to improve the homogeneity of the magnetic field without influencing each other. We place 2 pads opposite each other at location A and C (further denoted as AC), as given in the previous section and calculate the optimal pad parameters for the combined setup. We can see that the target field error and CV drops even more from the results given in Table 3.6 and the resulting field shown in Figure 3.22, becomes more homogeneous. The permittivity-conductivity plot shown in Figure 3.23 has almost the same invariance to the conductivity as the plot for a single pad for the CV method, however, for the target field method we see some larger influence of the conductivity as well.

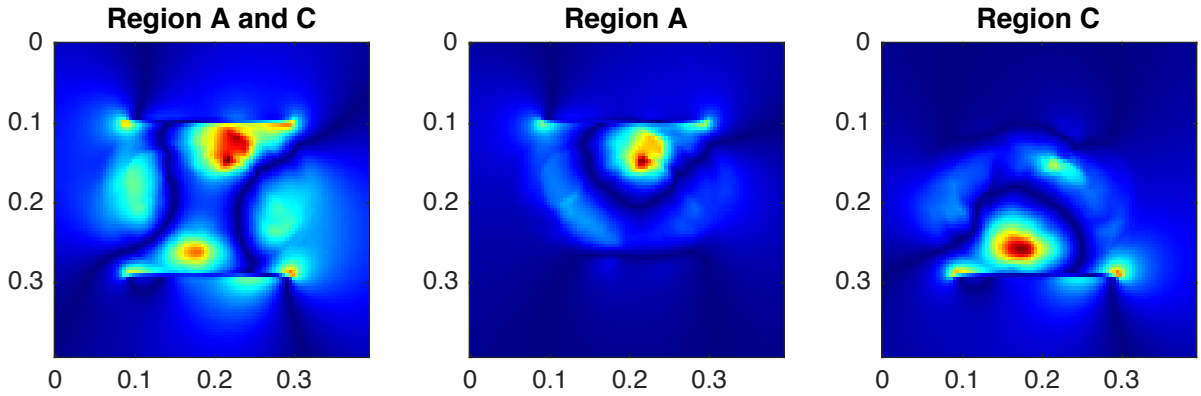

Figure 3.21: The region of influence a pad has, showed by subtracting the B_1^+ field with a pad from the B_1^+ field without a pad for pad locations AC, A and C respectively.

	ϵ_r^*	σ^*[S/m]	$err_B(\epsilon_r^*, \sigma^*)$	ϵ_r^*	σ^* [S/m]	$CV(\epsilon_r^*, \sigma^*)$
Location A and C	460	1.75	0.0025	400	1.00	12.7424%

Table 3.6: The optimal pad parameters for the different methods. The CV value for no pad present is 19.5073%

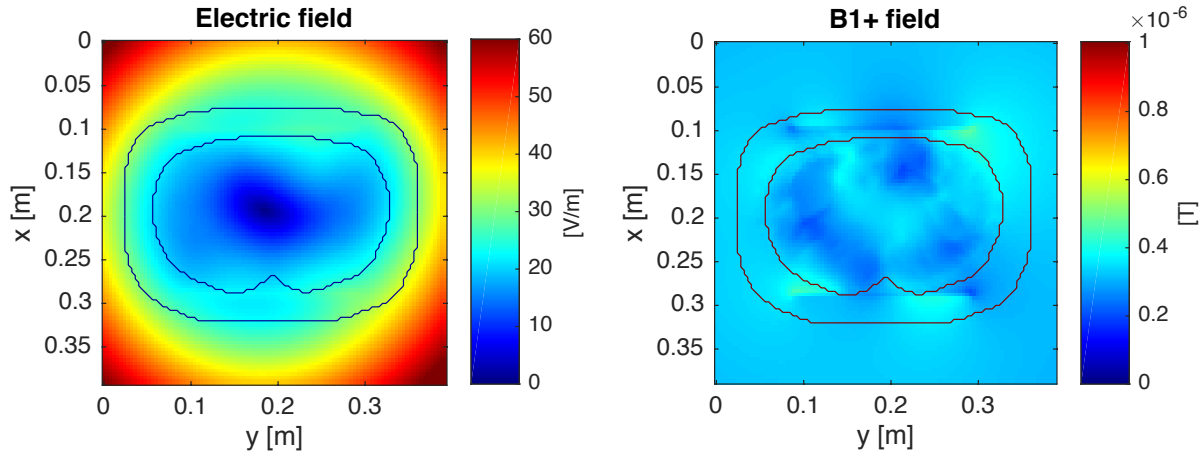

Figure 3.22: The resulting E and B_1^+ field respectively for the optimal pad parameters for the target field approach, where a pad is placed on location A and C. The resulting fields for the CV method are similar, since the optimal pad parameters are similar.

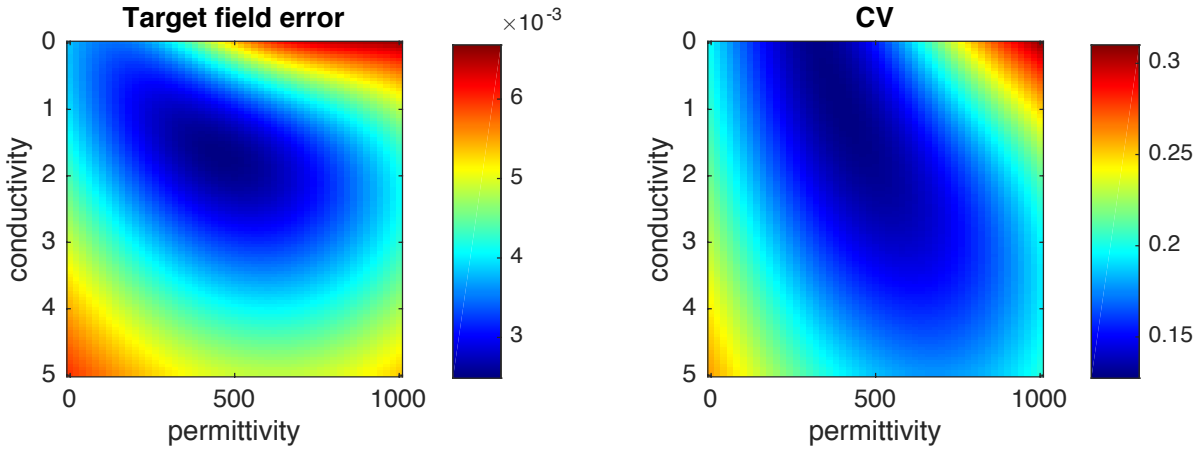

Figure 3.23: Permittivity-conductivity plot for pads placed at location A and C

Since there is almost no interaction between the 2 pads, we can also allow the 2 pads to have different permittivity and conductivity by simply select the 2 optimal pads from the previous section and use these to generate the B_1^+ field, instead of optimizing the pad parameters for the different pads in a single configuration, as done in [9]. This can also be seen when we compare the results from Table 3.6 with the results from Table 3.5. The optimal pad parameters for the 2 pads on location AC are similar to the optimal pad parameters for the individual pad A and pad C. Notice that the optimal permittivity of pad AC is close to pad A, while the optimal conductivity of pad AC is close to pad C.

3.6. Influence of pad shapes on the optimal pad parameters

In all previous simulations we have used a rigid rectangular shaped pad. However, in practice the pad is really flexible, and hence follows the contour of the body it is placed on. Figure 3.24 shows such deformable pad following the contour lines of the human body, were we made use of the 1 mm grid to get some more detail. We see very similar results for such a deformable pad, hence, the assumption the pad is rigid and rectangular shaped can be made for our simulations due to the close position of the rectangular pad to the subject. A comparison between the results for the rigid pad, as used before and the deformable pad is made in Table 3.7.

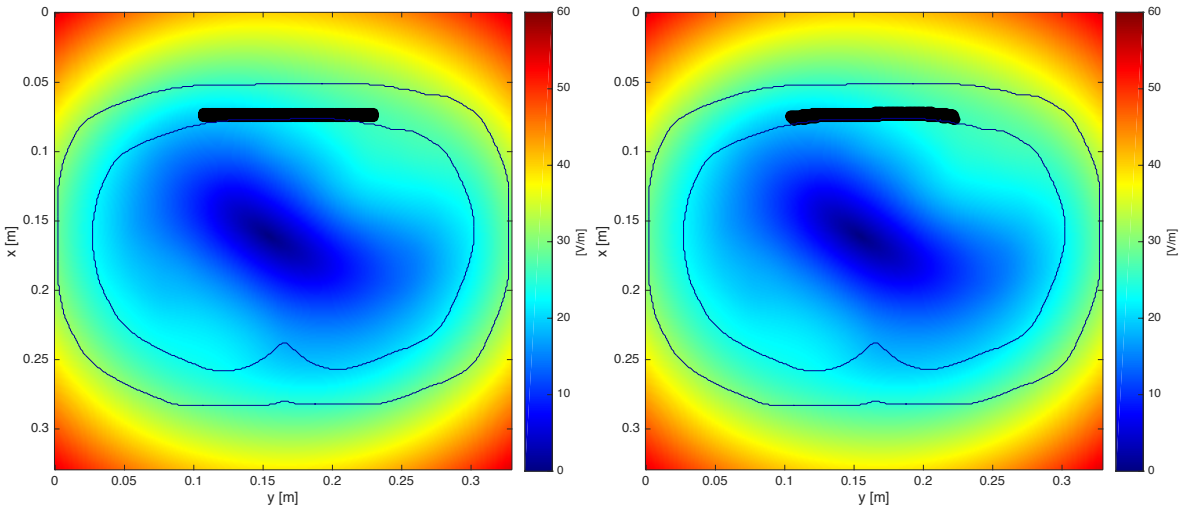

(a) Rigid rectangular shaped pad

(b) Deformable pad

Figure 3.24: The electric field on an 1 mm grid for more detail with a rigid pad (a) and a deformable pad following the contour lines of the body (b).

	ϵ_r^*	σ^*[S/m]	$err_B(\epsilon_r^*, \sigma^*)$	ϵ_r^*	σ^*[S/m]	$CV(\epsilon_r^*, \sigma^*)$
Rigid pad	600	2.95	$7.2684\ 10^{-4}$	580	2.60	15.0178%
Deformable pad	580	2.85	$7.3319\ 10^{-4}$	560	2.45	15.1410%

Table 3.7: Results for a deformable pad compared to the results we had before for a rigid pad, CV is 20.1509% in case no pad present.

Another option is to divide the pad in separate parts to prevent all effects of induced currents in the pad itself. The results of the different pad shapes as shown in Figure 3.25 are given in Table 3.8. From the results for the CV method we can see that pad 1 (a pad without holes) has the lowest error. Obviously, induction currents in the pad are not likely in a 2D simulation where the field is invariant in the z-direction. Therefore, these pad shapes can only be of use in 3D.

The target field method where the 2-norm is taken shows a more robust error measure and is therefore not changing for the different pad shapes. Notice the increase in optimal pad parameters to compensate for pads with larger gaps, this property will be explored in further detail in the next section.

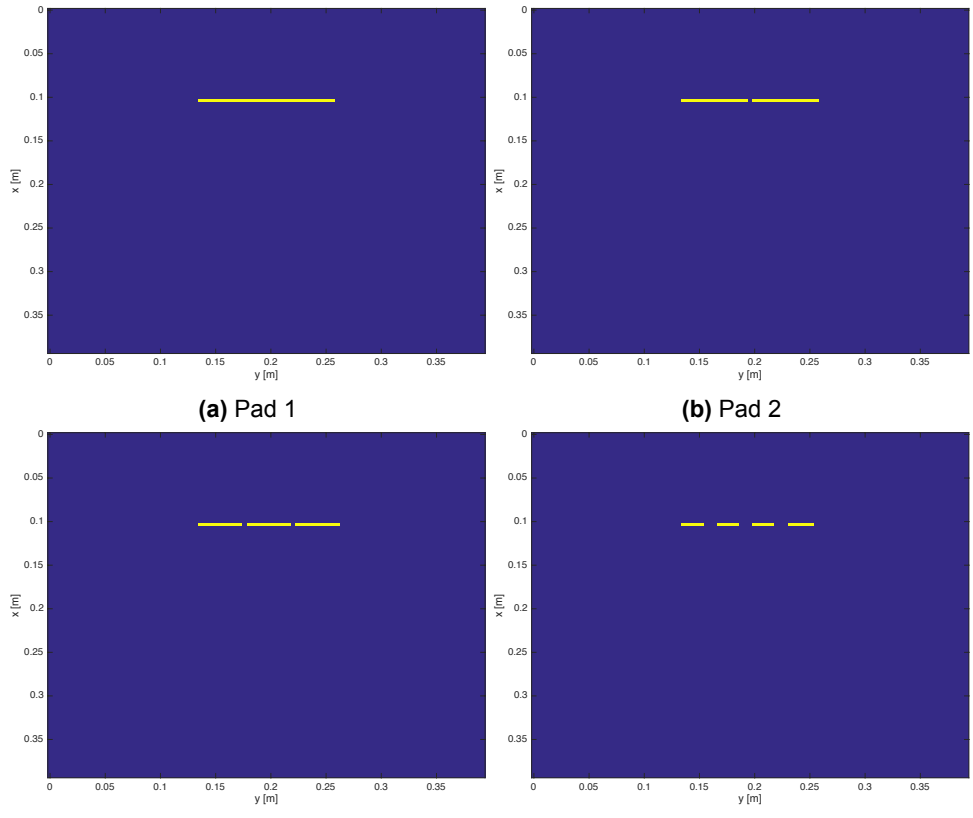

(a) Pad 1 **(b)** Pad 2

(c) Pad 3 **(d)** Pad 4

Figure 3.25: Different pad designs, where pad 1 is the same pad as used before.

	ϵ_r^*	σ^*[S/m]	$err_B(\epsilon_r^*, \sigma^*)$	ϵ_r^*	σ^*[S/m]	$CV(\epsilon_r^*, \sigma^*)$
Pad 1	540	2.55	0.0029	540	2.55	14.9140%
Pad 2	580	2.95	0.0029	560	2.65	14.9411%
Pad 3	600	3.05	0.0029	580	2.8	14.9545%
Pad 4	840	4.2	0.0029	820	3.85	15.0306%

Table 3.8: Results for different pad designs, $CV = 19.5073\%$ in case no pad present.

3.7. The influence of the pad thickness

We will use the 1 mm grid again to simulate the effect of the number of layers on the optimal permittivity and conductivity, so we can compare the optimal pad parameters for a pad of 1 mm thickness up to 25 mm in steps of 1 mm. The results of this comparison for both target field method (the field inside the human body is used as target field with the 2-norm error) and CV are given in Table 3.9.

	Target Field method			CV		
#Layers	ϵ_r^*	σ^*[S/m]	$err_B(\epsilon_r^*, \sigma^*)$	ϵ_r^*	σ^*[S/m]	$CV(\epsilon_r^*, \sigma^*)$
1	2260	10.50	$7.3617\ 10^{-4}$	2140	8.65	15.1668%
2	1140	5.35	$7.3553\ 10^{-4}$	1080	4.45	15.1625%
3	760	3.60	$7.3513\ 10^{-4}$	720	3.00	15.1612%
4	580	2.80	$7.3479\ 10^{-4}$	540	2.30	15.1622%
5	460	2.25	$7.3465\ 10^{-4}$	440	1.90	15.1638%
6	400	1.95	$7.3473\ 10^{-4}$	360	1.55	15.1719%
7	340	1.70	$7.3470\ 10^{-4}$	320	1.45	15.1752%
8	300	1.50	$7.3485\ 10^{-4}$	280	1.25	15.1833%
9	260	1.30	$7.3511\ 10^{-4}$	260	1.20	15.1991%
10	240	1.20	$7.3547\ 10^{-4}$	220	1.00	15.2087%
11	220	1.15	$7.3598\ 10^{-4}$	200	0.95	15.2225%
12	200	1.05	$7.3638\ 10^{-4}$	200	0.95	15.2433%
13	180	0.95	$7.3709\ 10^{-4}$	180	0.90	15.2531%
14	180	0.95	$7.3827\ 10^{-4}$	180	0.90	15.3043%
15	160	0.85	$7.3840\ 10^{-4}$	160	0.80	15.2914%
16	160	0.85	$7.4012\ 10^{-4}$	140	0.70	15.3088%
17	140	0.75	$7.4027\ 10^{-4}$	140	0.70	15.3290%
18	140	0.75	$7.4147\ 10^{-4}$	120	0.60	15.3700%
19	120	0.70	$7.4318\ 10^{-4}$	120	0.60	15.3759%
20	120	0.65	$7.4347\ 10^{-4}$	120	0.65	15.4046%
21	120	0.65	$7.4475\ 10^{-4}$	120	0.65	15.4492%
22	120	0.65	$7.4719\ 10^{-4}$	100	0.55	15.4672%
23	100	0.60	$7.4764\ 10^{-4}$	100	0.55	15.4805%
24	100	0.60	$7.4853\ 10^{-4}$	100	0.55	15.5093%
25	100	0.55	$7.5005\ 10^{-4}$	100	0.55	15.5527%

Table 3.9: Optimal permittivity and conductivity values for both target field method and CV for varying thickness.

Notice from the results that the optimal parameter values drop when increasing the number of layers and accordingly the thickness of the pad. Both, permittivity and conductivity drop with an exponential decay, where the steepness is similar between permittivity and conductivity and also for the target field method and CV. This is shown for each parameter separately in Figure 3.26-3.27. When we take a closer look into the effect of the error, we see that the number of layers does not influence the error much as shown in Figure 3.28-3.29. For the target field method we see the smallest error for a five millimeter-thick pad and for the CV method we see the smallest CV for a three millimeter-thick pad. Around this optimum the error and CV are almost constant, but for a much thicker pad we again see an increase in the error and CV, resulting in a less homogeneous field. However, the increase in error for each extra layer is relatively small.

In practice, due to the almost invariance of the error and CV for different thicknesses the curves describing the optimal permittivity and conductivity with respect to the number of layers can be used in the process of designing and building an optimal pad. When an optimal pad is developed, however the designed permittivity is unreachable, the pad can be adapted easily in thickness so that the pad is still optimal for a reachable permittivity.

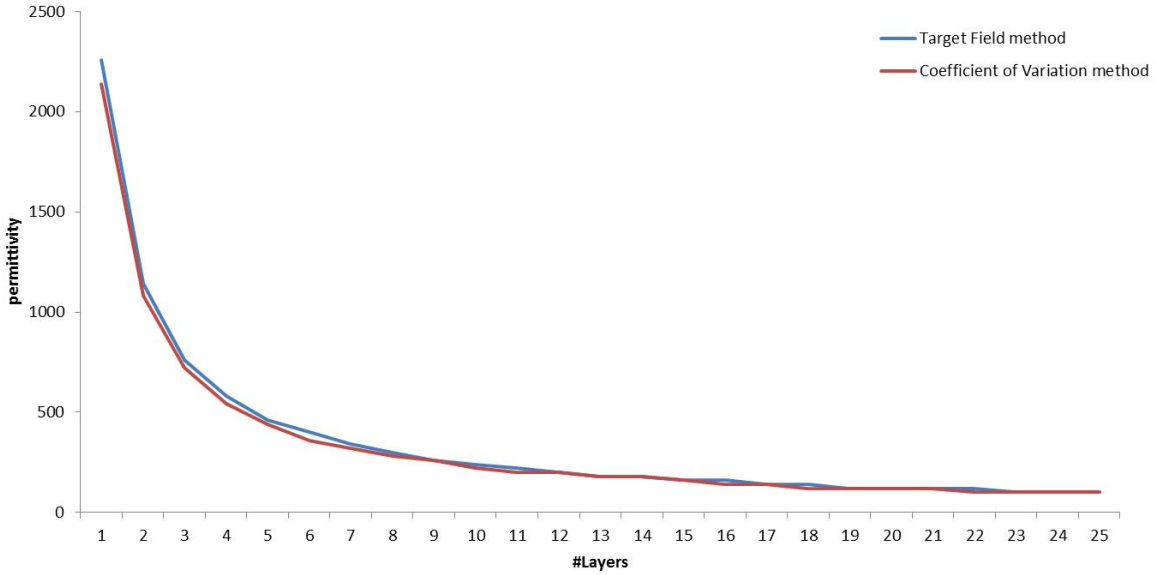

Figure 3.26: Plot of permittivity vs #layers for target field method and Coefficient of Variation method.

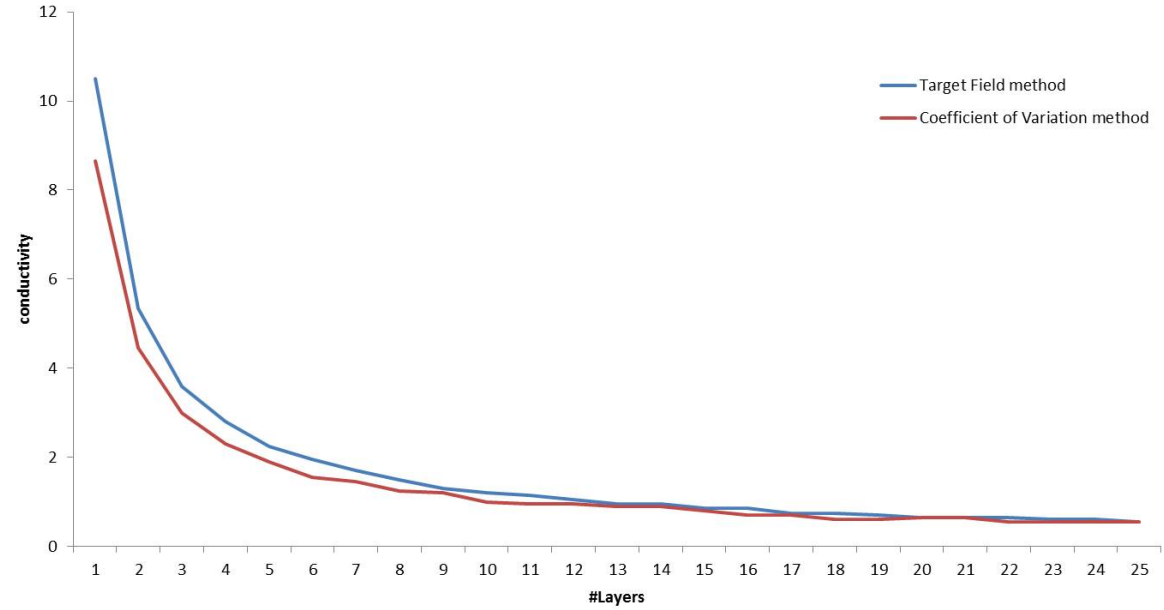

Figure 3.27: Plot of conductivity vs #layers for target tield method and Coefficient of Variation method.

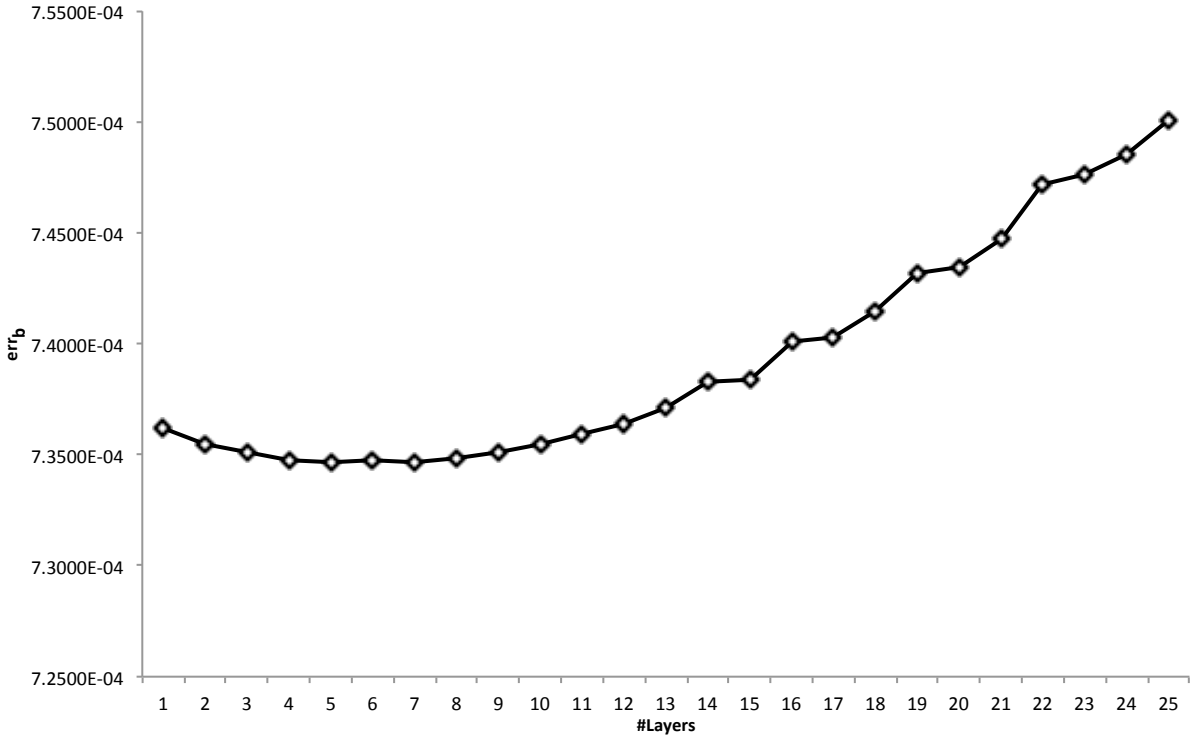

Figure 3.28: Plot of error vs #layers for target field method.

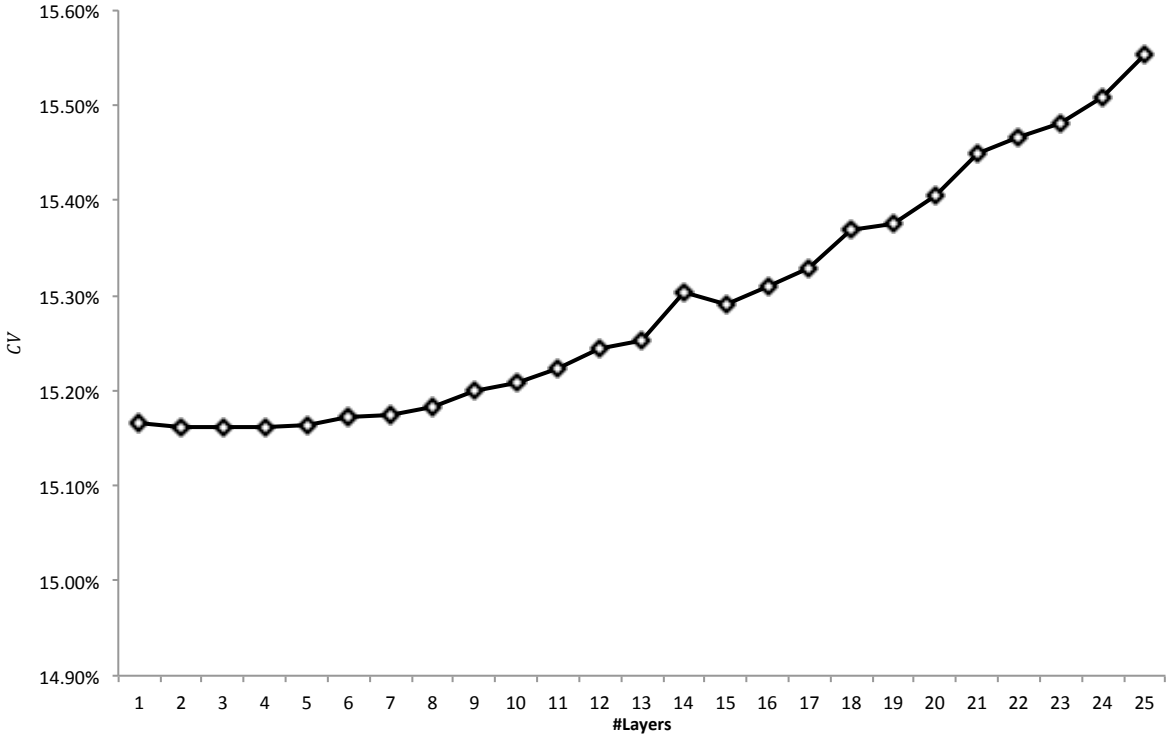

Figure 3.29: Plot of CV vs #layers for Coefficient of Variation method.

4

Analytical Optimization Approach

Using the approach in the previous chapter we have to solve a forward problem for every possible dielectric pad. This can be quite cumbersome and time consuming when scaling the problem to 3D or when adding more degrees of freedom (such as thickness, location, dimensions etc.). In this chapter we will use a more analytical approach in order to find the optimal permittivity and conductivity for a given pad, so we do not have to calculate all possible outcomes. A common used algorithm for this purpose is Gauss-Newton [13][11]. This algorithm follows an iterative approach where the model parameters are updated every iteration, such that the misfit between the desired field and the predicted field is minimized. We use a similar approach to describe the data mismatch, given by an objective function as we did in the previous chapter for the target field method. Furthermore, we can adjust the iterative step by using a backtracking algorithm in order to smooth the behaviour of the algorithm.

4.1. The objective Function

The objective function can be defined by a similar functional as the previously described functional for the target field method in Equation 3.2. The derivative of the objective function is needed in order to solve this nonlinear optimization problem, therefore, the 2-norm of the target field error will suit best. Taking this into account, the objective function results in

$$F(\chi) = \frac{\left\| \mathbf{B}_1^{+\text{desired}} - \mathbf{B}_1^{+}(\chi) \right\|_2^2}{\left\| \mathbf{B}_1^{+\text{desired}} \right\|_2^2}, \tag{4.1}$$

where χ is the parameter that needs to be optimized and describes the contrast of the pad, which can be written as a 2 parameter problem by noticing that the contrast of the pad in Equation 2.7 is given by a real and imaginary part and therefore χ can be written as

$$\chi = \chi_r + \mathrm{j}\chi_i. \tag{4.2}$$

Let us introduce the operator $\mathcal{K}$, independent of χ which transforms the electric E field to the B_1^+ field. This operator can easily be defined by Equation 2.15 and Equation 2.16, and furthermore, calculate the B_1^+ field with Equation 2.12. Accordingly, we write the objective function in terms of the electric field and calculate the gradient by introducing a first order distortion, with distortion term $\delta\chi$ as

$$F(\chi + \delta\chi) = \frac{\left\| \mathcal{K}\mathbf{E}^{\text{desired}} - \mathcal{K}\mathbf{E}(\chi + \delta\chi) \right\|_2^2}{\left\| \mathcal{K}\mathbf{E}^{\text{desired}} \right\|_2^2}. \tag{4.3}$$

4.2. The Phase Information

Notice that we do not only use the magnitude of the desired field and measured field given in Equation 4.1 as we did for the target field method in Chapter 3. The phase is also taken into account, so

that the derivative of the objective function can easily be calculated. This introduces a new problem, namely how to find a desired phase for the target field.

4.2.1. Backward Phase Update Method

The above described problem is already solved by updating the phase of the desired field iteratively, since the phase is slowly varying for different pad permittivity and conductivity values [22]. For the first iteration the phase of the background field is taken and the phase is updated iterative by taking the phase of the previous iteration of the predicted field as follows

$$F(\chi_k) = \frac{\left\| \left|\mathbf{B}_1^{+\text{desired}}\right| e^{j\boldsymbol{\varphi}(\chi_{k-1})} - \mathbf{B}_1^{+}(\chi_k) \right\|_2^2}{\left\| \left|\mathbf{B}_1^{+\text{desired}}\right| e^{j\boldsymbol{\varphi}(\chi_{k-1})} \right\|_2^2}, \tag{4.4}$$

where the subscript k labels the iteration. The phase of the desired field is the phase from the previous iteration of the measured field denoted as

$$\boldsymbol{\varphi}(\chi_{k-1}) = \text{phase}\left(\mathbf{B}_1^{+}(\chi_{k-1})\right), \tag{4.5}$$

with $\boldsymbol{\varphi}(\chi_0) = \text{phase}\left(\mathbf{B}_{1;\text{b}}^{+}\right)$ for the first iteration. For convenience, we call this method the Backward Phase Update (BPU) method from now on.

4.2.2. Forward Phase Update Method

In our proposed Forward Phase Update (FPU) method we calculate the phase of the initial field, $\mathbf{B}_1^{+}(\chi_0)$ or later the predicted field, $\mathbf{B}_1^{+}(\chi_k)$ of the current iteration first and use this instead of taking the phase of the previous iteration, as follows

$$F(\chi_k) = \frac{\left\| \left|\mathbf{B}_1^{+\text{desired}}\right| e^{j\boldsymbol{\varphi}(\chi_k)} - \mathbf{B}_1^{+}(\chi_k) \right\|_2^2}{\left\| \left|\mathbf{B}_1^{+\text{desired}}\right| e^{j\boldsymbol{\varphi}(\chi_k)} \right\|_2^2} = \frac{\left\| \left|\mathbf{B}_1^{+\text{desired}}\right| - \left|\mathbf{B}_1^{+}(\chi_k)\right| \right\|_2^2}{\left\| \left|\mathbf{B}_1^{+\text{desired}}\right| \right\|_2^2}, \tag{4.6}$$

where $\boldsymbol{\varphi}(\chi_k)$ is the phase of $\mathbf{B}_1^{+}(\chi_k)$. Hence, the phase of the current B_1^{+} field has to be determined before the objective function can be calculated, therefore, an extra calculation has to be made. On the other hand, we expect that the extra phase information will let the minimization procedure converge faster, since no alternate updating occurs between the phase and the magnetic field.

4.3. The Gauss-Newton Minimization Approach

To solve the above nonlinear optimization problem, we use a Gauss-Newton minimization approach which makes use of a local quadratic model of the objective function. The model is obtained by taking the terms up to the second order of the Taylor-series expansion of the objective function as follows

$$F(\chi_r + \delta\chi_r, \chi_i + \delta\chi_i) = F(\chi_r, \chi_i) + \mathbf{g}_\chi^T \delta\mathbf{z} + \frac{1}{2}\delta\mathbf{z}\mathbf{H}_\chi\delta\mathbf{z} + \text{higher order terms}, \tag{4.7}$$

where $\delta\mathbf{z} = [\delta\chi_r, \delta\chi_i]^T$. The gradient is given by

$$\mathbf{g} = -c\,\text{Re}\left[\mathbf{J}^H\mathbf{r}(\chi_r, \chi_i)\right], \tag{4.8}$$

where $c = 2\left|\mathcal{K}\mathbf{E}^{des}\right|^{-2}$ is a scaling factor and $\mathbf{r}(\chi_r, \chi_i) = \mathcal{K}\mathbf{E}^{\text{desired}} - \mathcal{K}\mathbf{E}(\chi_r, \chi_i)$ denotes the residual. Furthermore, the reduced Hessian is written as

$$\mathbf{H} = c\mathbf{J}^H\mathbf{J}. \tag{4.9}$$

with $\mathbf{J} = \left(\mathbf{I} + \chi\mathbf{Z}\mathbf{A}^{-1}\mathbf{S}^T\right)\mathbf{Z}\mathbf{A}^{-1}\mathbf{S}^T\mathbf{e}$. The derivations are given in more detail in Appendix C. The Gauss-Newton update direction is now given by

$$\delta\mathbf{z} = -\mathbf{H}^{-1}\mathbf{g} = \left(\mathbf{J}^H\mathbf{J}\right)^{-1}\text{Re}\left[\mathbf{J}^H(\chi_r, \chi_i)\right]. \tag{4.10}$$

4.4. Backtracking

We introduce a step length ν in order to obtain a sufficient decrease in the objective function in the direction $\delta\mathbf{m}$. So the update is given by

$$\mathbf{z}_k = \mathbf{z}_{k-1} + \nu\delta\mathbf{z}_k. \tag{4.11}$$

A sufficient decrease of the objective function is described by the so-called Armijo condition as

$$F(\mathbf{z} + \nu\delta\mathbf{z}) \leq F(\mathbf{z}) + \alpha\nu\mathbf{g}^T\delta\mathbf{z}, \tag{4.12}$$

where α is a small positive number (usually one sets $\alpha = 10^{-4}$). We follow the standard backtracking algorithm to calculate the update of the step length iteratively until the Armijo condition is satisfied [18][2][13].

4.5. Results

First, we will again use a known target field created by a pad placed on a fixed position with a relative permittivity, $\epsilon_r^{\text{pad}} = 500$ and a conductivity, $\sigma^{\text{pad}} = 3$ S/m. We use the magnitude of this field to test the Gauss Newton method where we choose the starting parameters close to the parameter values of the target field. Initially, we assume the phase is known, hence we use the actual phase of the target field. From Figure 4.1a we see that the pad parameters converge quickly to the true values. After 2 iterations the algorithm is already converged and after 6 iterations it has reached the stopping criteria

$$|\chi_k - \chi_{k-1}| < 10^{-8},$$

we denote ϵ_r^* and σ^* as the optimal pad parameters found after reaching the stopping criteria.

Now that we have shown that the Gauss Newton method converges to the optimal solution ($\epsilon_r^{\text{pad}} = \epsilon_r^*$ and $\sigma^{\text{pad}} = \sigma^*$), we can test the algorithm for a more realistic case where the phase of the desired field is not known. We test the methods proposed in Section 4.2 in combination with the backtracking procedure as described in Section 4.4. The BPU method is not converging when we do not use backtracking, as can be seen from the results in Table 4.1 and Figure 4.1b. The algorithm lost track in the first iteration already due to the mismatch of the phase of the background field (chosen to be the initial phase of the desired field) and the actual phase of the predicted field.

By using the backtracking procedure we prevent the algorithm to loose track as shown in Figure 4.1c. Still, we can notice the effect of the phase mismatch in the first iteration and after every odd number of iterations where the parameter values are pushed back due to the lagging phase. Notice that this procedure does not converge to the optimal pad parameters after 10 iterations, since, the area around the optimal pad parameters forms a valley as already shown in Chapter 3. Therefore, the gradient becomes very small and so does the step length ν. We have to guard against too small values for ν by setting $\nu_{min} = 0.1$ to prevent from excessively slowing down the iterative process. There is still very little progress towards the minimum, even with setting ν to ν_{min} when it decreases below 0.1 and proceeds with the iteration, hence the stopping criterion is already reached after 10 iterations and the process is terminated.

Method	# iterations	ϵ_r^*	σ^* [S/m]	$F(\epsilon_r^*, \sigma^*)$
Actual phase	6	500.00	3.00	5.9135 10^{-31}
BPU	30	10217.14	-38.22	0.1557
BPU + backtracking	10	479.31	2.91	4.4626 10^{-5}
FPU	30	499.97	2.99	1.7110 10^{-10}

Table 4.1: The results for $\epsilon_{r_0} = 450$ and $\sigma_0 = 2.7$ S/m after maximum 30 iterations, with the target field created by a pad with $\epsilon_r^{\text{pad}} = 500$ and $\sigma^{\text{pad}} = 3$ S/m.

Based on these results we came up with our own proposed FPU method, as described above, which smoothly converges to the true values as shown in Figure 4.1d. In this case the algorithm decreases sufficiently, the Armijo condition is already satisfied with $\nu = 1$ for every iteration, so the backtracking

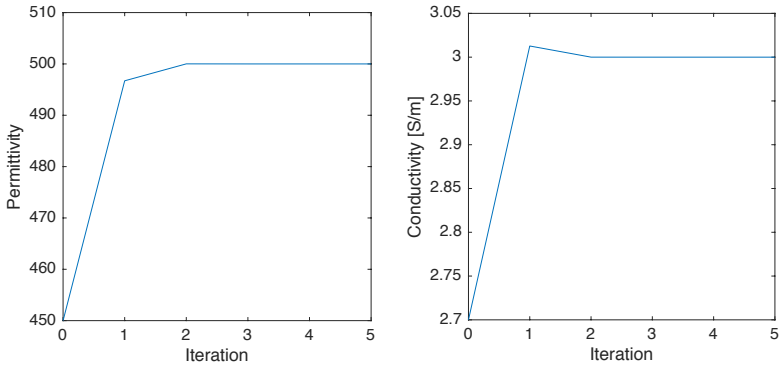

(a) Actual phase

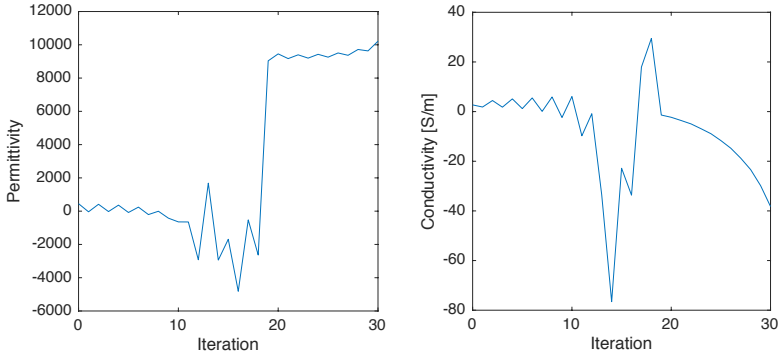

(b) BPU method

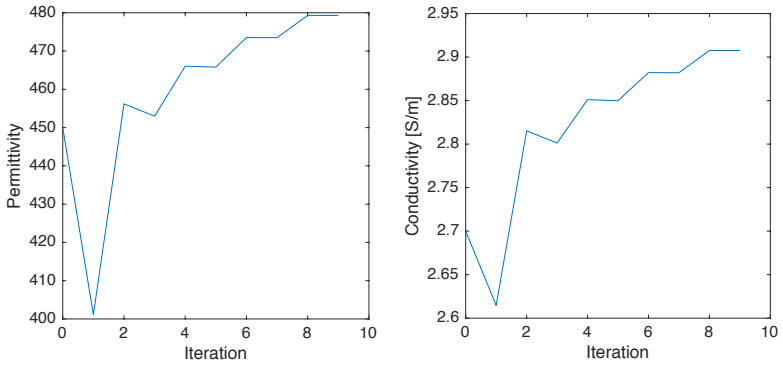

(c) BPU method + backtracking

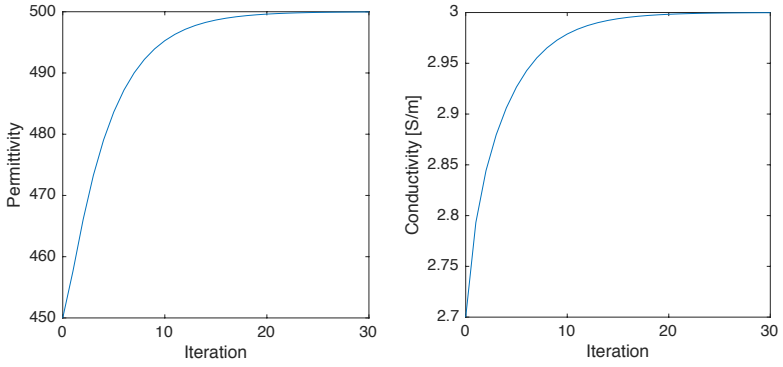

(d) FPU method

Figure 4.1: The permittivity and conductivity at every iteration for the different methods, where $\epsilon_{r0} = 450$ and $\sigma_0 = 2.7$. The target field is created by a pad with $\epsilon_r^{\text{pad}} = 500$ and $\sigma^{\text{pad}} = 3$ S/m.

algorithm will never be used. The process is terminated when it reaches 30 iterations, the maximum number of iterations set.

When we use a pad with different dimensions we more clearly see the effect of backtracking, since the pad parameter values stay positive for each iteration, hence the Gauss Newton method keeps more or less track and converges. An example is shown in Figure 4.2.

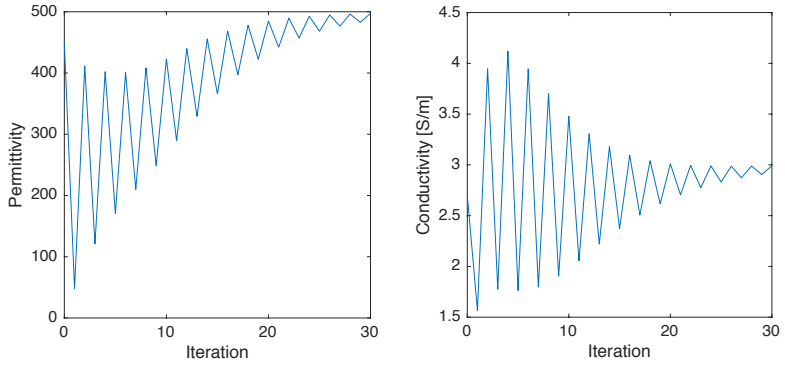

(a) Backtracking disabled

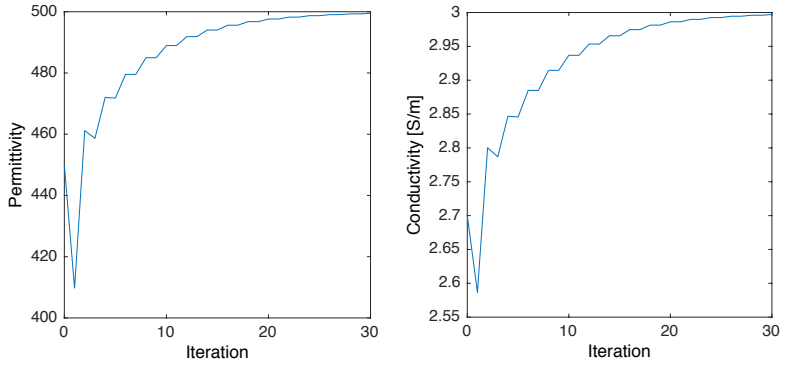

(b) Backtracking enabled

Figure 4.2: An illustration of the effect of backtracking.

Instead of an initial guess close to the optimal values, we now assume that we do not know where the optimal values are located. Therefore, we start with initial values of $\epsilon_{r0} = 1$ and $\sigma_0 = 0$ S/m, those values are equal to the case no pad present (background field only). Again, we first look at the scenario when the actual phase is known. We can see from the results in Table 4.2 and from Figure 4.3a that the method needs one extra iteration to converge and 2 extra iterations to reach the stopping criteria. This is in line with our expectations, more steps are needed since the starting position is located further away from the optimal values.

Method	# iterations	ϵ_r^*	σ^* [S/m]	$F(\epsilon_r^*, \sigma^*)$
Actual phase	8	500.00	3.00	$2.1824\ 10^{-31}$
BPU	30	479.14	2.91	$4.6500\ 10^{-5}$
BPU + backtracking	30	479.53	2.91	$4.4567\ 10^{-5}$
FPU	30	499.51	3.00	$4.0781\ 10^{-8}$

Table 4.2: The results for $\epsilon_{r0} = 1$ and $\sigma_0 = 0$ S/m after maximum 30 iterations, with the target field created by a pad with $\epsilon_r^{\text{pad}} = 500$ and $\sigma^{\text{pad}} = 3$ S/m.

Since the initial values are equal to the contrast of the background field, backtracking is not necessary for the BPU method, hence no mismatch between the phase of the desired and measured B_1^+ occurs in the first iteration. The process keeps track as can be seen in Figure 4.3b, which is similar to Figure 4.3c, the case where backtracking is used. We still can see the fallback introduced by the lagging phase update every alternating iteration step. When we compare both results we can see that

backtracking prevents for fall backs, however the convergence is still slowing down every second iteration step, therefore the overall convergence speed is not increasing. For our proposed method we again see a smooth convergence as shown in Figure 4.3d and from Table 4.2 we see that the final result approximates more closely the target field values.

In practice the target field is not a field generated by a pad. Instead, we create a desired field that describes a homogeneous field with a field strength useful in practice and an unknown phase. We use the same target field as described in Section 3.3.2 and for the phase we use the 2 different phase update methods. From the results in Table 4.3 we see similar results for the different approaches after 30 iterations. Figure 4.4 shows the difference between the two methods and the effect of backtracking again, which are similar to to the previous results. Notice that those results are for a homogeneous field defined over the full grid instead of a homogeneous field inside the object only. In practice however, we are only interested in a homogeneous field inside the subject. The norm of objective function given in Equation 4.1, can defined for points inside the subject only.

Method	# iterations	ϵ_r^*	σ^* [S/m]	$F(\epsilon_r^*, \sigma^*)$
BPU	30	320.68	1.79	0.0073
BPU + backtracking	30	321.20	1.80	0.0073
FPU	30	330.02	1.87	0.0073

Table 4.3: Results for a homogeneous target field after maximum 30 iterations with $\epsilon_{r0} = 1$ and $\sigma_0 = 0$ S/m.

The results for the field inside the subject only are given in Table 4.4. Those results show that the BPU method converges to the same value with and without backtracking. For our proposed method we see for the first time that the Armijo conditions are not always satisfied, hence the backtracking routine is used. The optimization routine converges as well to similar values as the values we had for the BPU method, but the stopping criteria are reached in already 16 iterations. The FPU method without backtracking converges to higher parameter values after 30 iterations. Furthermore, we relax the stopping criteria in order to test if the Gauss Newton method has reached the optimum after 30 iterations already, what seems to be from the plotted results in Figure 4.5. Therefore, the maximum number of iterations is increased to 60. For the FPU method this results in optimal pad values very similar to the values we had after 30 iterations, namely $\epsilon_r^* = 561.96$ and $\sigma^* = 2.84$ S/m. However, for the BPU method we see that the pad further converges towards the same values of our proposed method, namely $\epsilon_r^* = 561.08$ and $\sigma^* = 2.83$ S/m. While for both methods with backtracking we obviously do not see further convergence.

Method	# iterations	ϵ_r^*	σ^* [S/m]	$F(\epsilon_r^*, \sigma^*)$
BPU	30	535.79	2.70	0.0219
BPU + backtracking	30	532.39	2.68	0.0219
FPU	30	561.19	2.83	0.0283
FPU + backtracking	16	532.41	2.68	0.0219

Table 4.4: Results for a homogeneous target field inside the human body after maximum 30 iterations with $\epsilon_{r0} = 1$ and $\sigma_0 = 0$ S/m.

Finally, we can compare these results with the result we got by inspection, as described in Chapter 3. We see very similar results when we compare the optimal pad values form Table 4.4 with the optimal permittivity and conductivity for the 2-norm target field error for a pad located at the same position and with the same size, as denoted in Table 3.3 ($\epsilon_r^* = 560$ and $\sigma^* = 2.85$ S/m). Especially, the results for our proposed FPU method without backtracking converge to the same values. That the method with backtracking converges earlier to lower values can be explained from the results obtained by inspection. There we have noticed that the optimal permittivity and conductivity are found in a valley, hence the gradient is almost zero and the backtracking procedure achieves very little process. For the BPU we see similar results, hence with a much slower convergence speed.

The total number of iterations, mostly determines the amount of time needed to reach the optimal pad parameter values. To give some indication of time, we measured the executing time of our Matlab

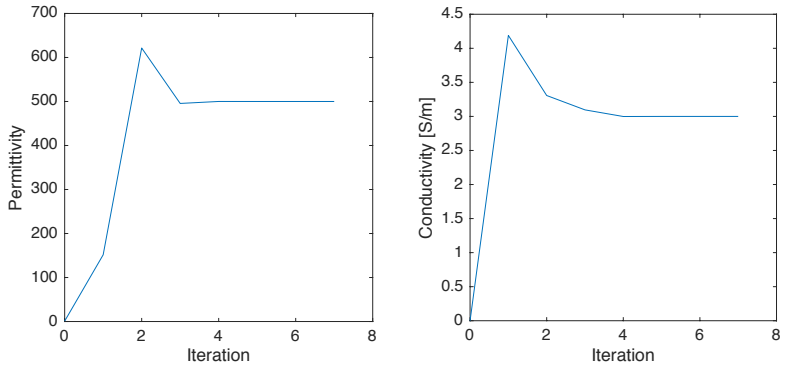

(a) Actual phase

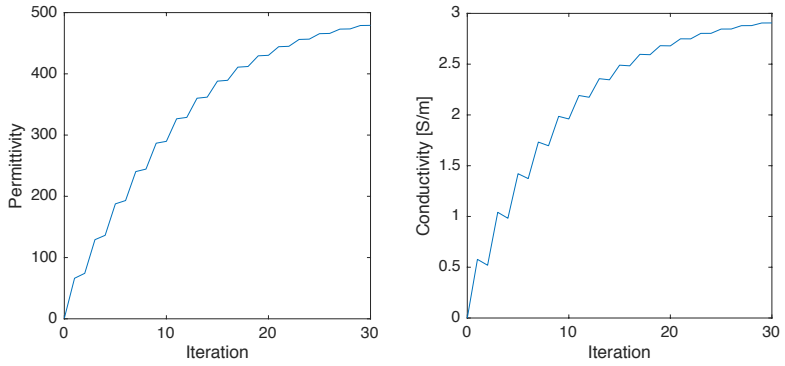

(b) BPU method

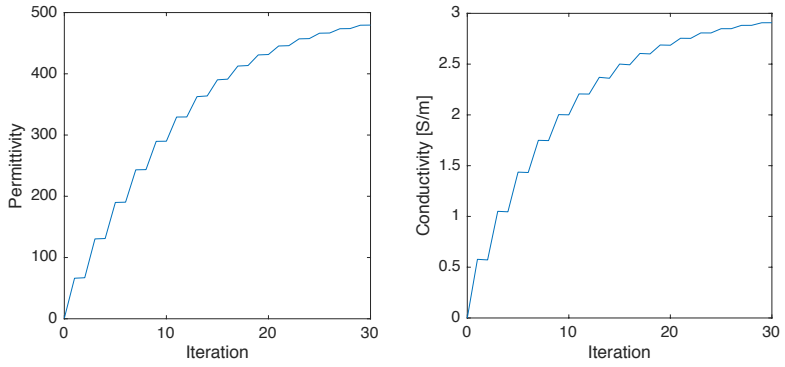

(c) BPU method + backtracking

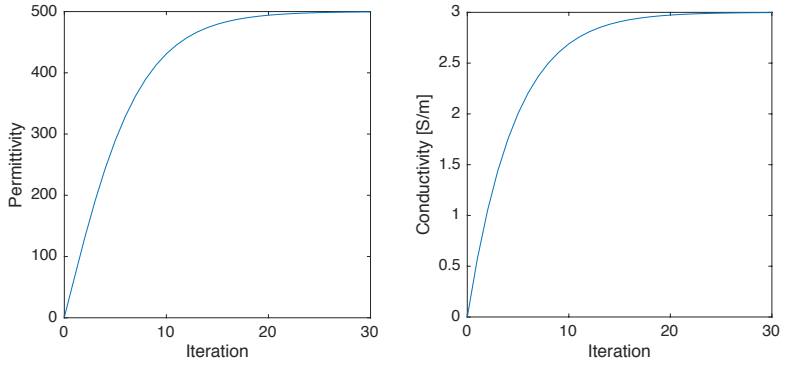

(d) FPU method

Figure 4.3: The permittivity and conductivity at every iteration for the different methods, where $\epsilon_{r0} = 1$ and $\sigma_0 = 0$. The target field is created by a pad with $\epsilon_r^{\text{pad}} = 500$ and $\sigma^{\text{pad}} = 3$ S/m.

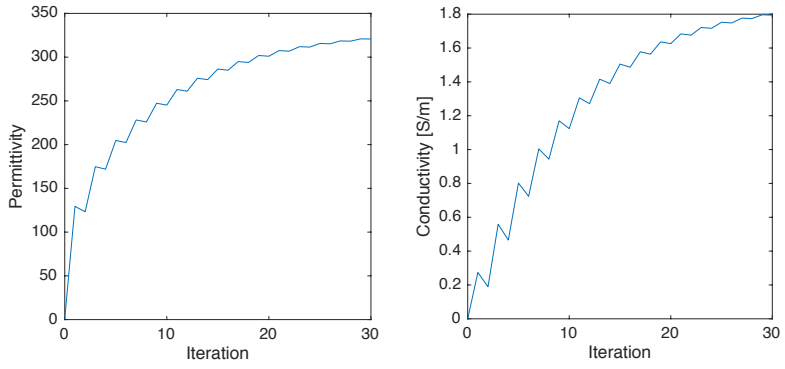

(a) BPU method

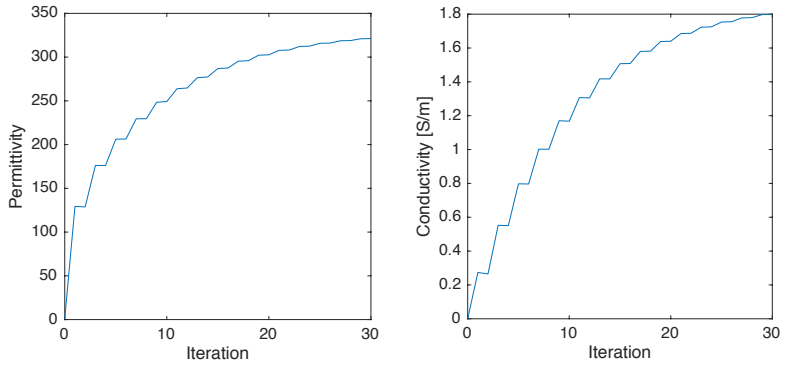

(b) BPU method + backtracking

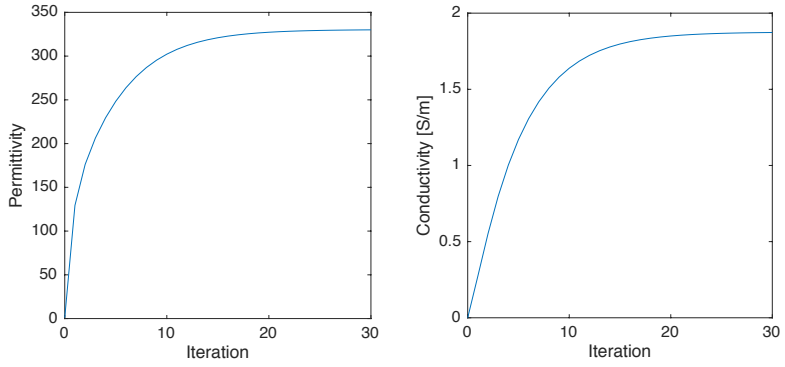

(c) FPU method

Figure 4.4: The permittivity and conductivity at every iteration for the different methods, where $\epsilon_{r0} = 1$ and $\sigma_0 = 0$. The target field is homogeneous.

script for the results in Table 4.4 on a Windows 7 64-bit computer with an Intel Core i5-4690 CPU @ 3.50 GHz and 8 GB of RAM. We noticed no significant difference in run time between the BPU and FPU method after 30 iterations, which took 79.9 seconds and 79.7 seconds respectively. When backtracking is enabled it took 77.1 seconds for the BPU method with 30 iterations and only 39.7 seconds for the FPU method, because it already converged after 16 iterations. From this results we can see that indeed the number of iterations determine the run time.

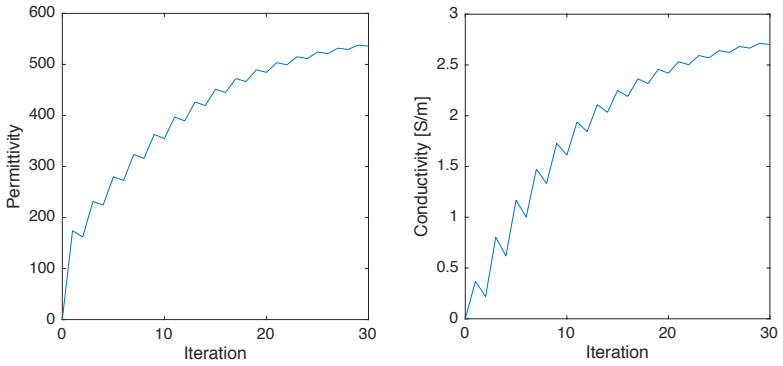

(a) BPU method inside subject

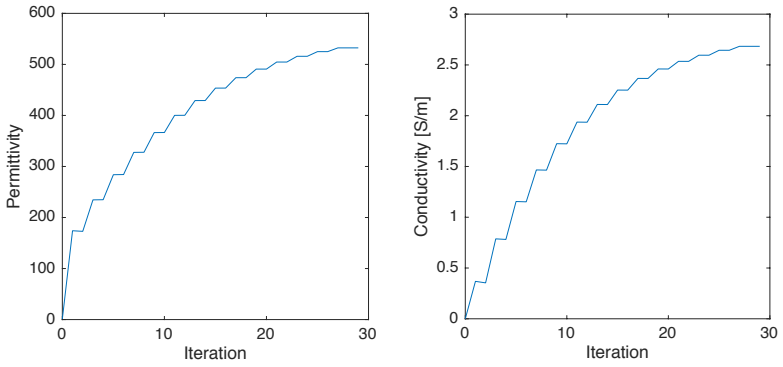

(b) BPU method inside subject + backtracking

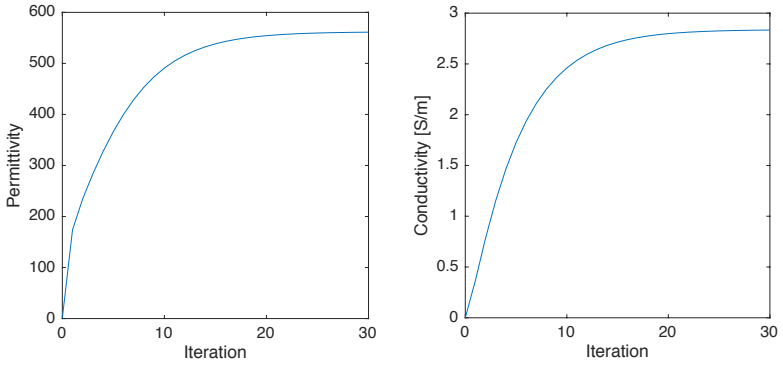

(c) FPU method inside subject

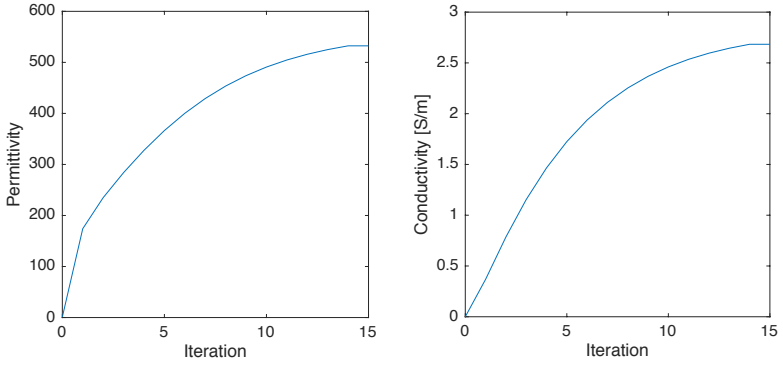

(d) FPU method + backtracking

Figure 4.5: The permittivity and conductivity at every iteration for the different methods, where $\epsilon_{r0} = 1$ and $\sigma_0 = 0$. The target field is homogeneous inside the human body.

5 Conclusions

Some final conclusions can be drawn from the results we obtained for the two different approaches we used to determine the optimal permittivity and conductivity for a dielectric pad. This is done by comparing the method via inspection with the Gauss-Newton method in Section 5.1, furthermore, we will give some general pad designing remarks in Section 5.2. Finally, in Section 5.3 we will give some suggestions for future work that can be done.

5.1. Comparison

One fundamental difference between the two techniques is that the Gauss-Newton method needs a functional that is differentiable, hence the choice of objective function we want to to minimize is limited. For the method via inspection this is not necessary, therefore we could use the CV and the target field method with different norms and desired fields, as functional. One of the largest difficulties in finding the optimal pad parameters is to measure the homogeneity of the B_1^+ field and accordingly, prescribing a desired field. The method via inspection gives us more freedom in selecting a best suited manner to measure the homogeneity of the B_1^+ field, since we are able to select a different functional. Therefore, this method is more flexible compared to the Gauss-Newton method.

The desired field for the Gauss-Newton method consists of both magnitude and phase information, in order to make the objective function for the Gauss-Newton method easily differentiable. Describing a desired phase is hard, however, the phase is slowly changing for different permittivity and conductivity values of the pad. Hence, the phase can be updated iteratively due to the iterative scheme of the Gauss-Newton method. Updating the phase with the common used BPU method slows down the Gauss-Newton method and phase mismatches can occur. Our proposed FPU method overcomes these problems by calculating the phase forwards. The method via inspection does not rely on any phase information, hence this method is more robust.

When we compare the speed of both methods, we have noticed that the method via inspection is very fast for a small pad and a few grid points, however, for an increased grid resolution to 1 mm, resulting in 16 times more grid points we already have seen a significant increase in the amount of time to find the optimal permittivity and conductivity. Therefore, expanding this method to a 3D scenario, hence resulting in more grid points will slow down this method even more drastically. On the other hand, increasing the number of points affects the Gauss-Newton method less since it will converge in the same number of iterations. Only the computation time of each iteration will increase due to the increased number of points, which will affect the time needed to calculate the inverse of the approximated Hessian.

This leads us to another difference between the two methods. Where the method via inspection fully profits from the Sherman-Morrison-Woodbury approach formulated by Equation 2.11, namely all the calculated inverses are of the size defined by the number of grid points occupied by the pad. While we see for Gauss-Newton in Equation 4.10 that the size of the inverse of the reduced Hessian is determined by the total number of grid points. Hence, the usage of Sherman-Morrison-Woodbury is more beneficial for the method via inspection.

The method via inspection (with the 2-norm target field method) and the Gauss-Newton method

result in very similar optimal pad permittivity and conductivity values as we already mentioned in Section 4.5, however, the approaches are fundamentally different. The method via inspection gives a better insight in how the permittivity and conductivity of a dielectric pad effects the homogeneity of the B_1^+ field and how permittivity and conductivity are related to each other, since the effect on the homogeneity of the B_1^+ field is plotted for a range of permittivity and conductivity values. Therefore, most remarks in the next section are based on the results obtained by simulations we did for different pad configurations with the method via inspection.

We can conclude that both optimization techniques for dielectric pads are able to find an optimal pad for a given location much faster since we reduced the order of the problem to great extent.

5.2. Pad Design Remarks

During our work we have developed some insight in pad design due to the different simulations we have done. We have seen that it is only useful to place pads close to regions with low signal in order to increase the homogeneity of the B_1^+ field and that pads placed far apart do not effect each other significantly.

Another interesting observation is the relation between the thickness of the pad and the optimal permittivity and conductivity. This relation can be described by a curve with an exponential decay, where thin pads have very high permittivity and conductivity values. Pad designers can benefit from this curve by selecting the optimal permittivity and conductivity values that are desirable for a pad and adapt the thickness, since the homogeneity of the B_1^+ field is almost the same for all pad thickness levels. Furthermore, a relation between the permittivity and conductivity can be seen from all the different permittivity-conductivity plots we have made in Chapter 3, from which we can see that a variation in permittivity affects more the homogeneity of the B_1^+ field than a variation in conductivity around the optimum.

From the simulation results for both the 1 mm grid and 4 mm grid we have seen that there are no benefits in pad design due to an increase in resolution. Therefore, we can conclude that a 4 mm grid is the preferred resolution, since the reduced number in points, and hence the gain in speed.

5.3. Future Work

Due to the limited time there is still work that needs to be done. First of all, the described methods need to be tested on different transverse body slices, for example a slice through the brain. The dimensions and electric properties of the brain are different from the abdominal region, therefore, probably different relations between permittivity and conductivity can be found. The effect of the frequency on the optimal pad parameters can also be examined, since all the simulations are made for a 3T MRI scanner.

As we have seen in Chapter 3, there are more pad parameters that affect the homogeneity of the B_1^+ field, e.g. pad location and dimensions, where we can take a look upon instead of permittivity and conductivity values only.

Furthermore, we can look if pads with varying permittivity and conductivity instead of using homogeneous pads, can increase the homogeneity of the B_1^+ even more. Besides that, we live in a three-dimensional world, a pad will have three dimensions placed on a three-dimensional human body. Therefore, the methods need to be extended to 3D such that simulations can be used in practice, where also SAR values need to be simulated for safety. The Gauss-Newton is the most suitable method for this extension, since the speed of this method depends less on the number of points.

However, the speed of the method via inspection can further improved by using a coarse-to-fine approach. A coarse scale of only permittivity values can be used first to find the optimal permittivity value. Subsequently, fine tune the scale in the range of the coarse optimal permittivity and determine the optimal permittivity and conductivity on the fine scale. This approach can reduce the number of calculations, since the B_1^+ field has to be calculated for less permittivity and conductivity values.

Our proposed FPU method needs some mathematical proof why the algorithm still converge when we take the phase of the current predicted B_1^+ field. The Rytov approximation [10] could be a good starting point for future research on this topic.

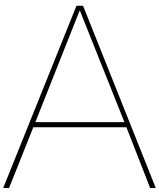

Abbreviations

BPU Backward Phase Update

CV coefficient of variation

FFT Fast Fourier Transform

FPU Forward Phase Update

MR Magnetic Resonance

MRI Magnetic Resonance Imaging

RF Radio Frequency

ROI region of interest

SAR Specific Absorption Rate

SNR Signal to Noise Ratio

B

The 2D discretization of the electromagnetic field

The discretization is done in the frequency domain, so the time-harmonic Maxwell's equations are again used as starting point

$$-\boldsymbol{\nabla}\times\hat{\mathbf{H}}+\sigma\hat{\mathbf{E}}+\mathrm{j}\omega\epsilon_0\hat{\mathbf{E}}=-\hat{\mathbf{J}}^{\text{ext}}, \tag{B.1}$$

and

$$\boldsymbol{\nabla}\times\hat{\mathbf{E}}+\mathrm{j}\omega\mu\hat{\mathbf{H}}=\mathbf{0}. \tag{B.2}$$

Let the configuration of interest be invariant in the z-direction and E-polarized, since it has been shown that this corresponds well to the field in the midplane of a MRI body coil.

These fields are governed by the equations

$$-\frac{\partial}{\partial x}\hat{H}_y+\frac{\partial}{\partial y}\hat{H}_x+\sigma\hat{E}_z+\mathrm{j}\omega\epsilon\hat{E}_z=-\hat{J}_z^{\text{ext}}, \tag{B.3}$$

$$\frac{\partial}{\partial y}\hat{E}_z+\mathrm{j}\omega\mu\hat{H}_x=0, \tag{B.4}$$

and

$$-\frac{\partial}{\partial x}\hat{E}_z+\mathrm{j}\omega\mu\hat{H}_y=0. \tag{B.5}$$

We use a scattering formalism to determine this electromagnetic field. Let the background field be the field in absence of the human body, the scatter source. The background field satisfies the equations

$$-\frac{\partial}{\partial x}\hat{H}_{y;\mathrm{b}}+\frac{\partial}{\partial y}\hat{H}_{x;\mathrm{b}}+\mathrm{j}\omega\epsilon\hat{E}_{z;\mathrm{b}}=-\hat{J}_z^{\text{ext}}, \tag{B.6}$$

$$\frac{\partial}{\partial y}\hat{E}_{z;\mathrm{b}}+\mathrm{j}\omega\mu\hat{H}_{x;\mathrm{b}}=0, \tag{B.7}$$

and

$$-\frac{\partial}{\partial x}\hat{E}_{z;\mathrm{b}}+\mathrm{j}\omega\mu\hat{H}_{y;\mathrm{b}}=0. \tag{B.8}$$

Now the scatter source occupies the bounded object domain $\mathbb{D}_{\text{obj}}$ in the (x,y)-plane. Inside the scatterer, the total field satisfies

$$-\frac{\partial}{\partial x}\hat{H}_y+\frac{\partial}{\partial y}\hat{H}_x+\sigma\hat{E}_z+\mathrm{j}\omega\epsilon\hat{E}_z=0, \tag{B.9}$$

$$\frac{\partial}{\partial y}\hat{E}_z+\mathrm{j}\omega\mu\hat{H}_x=0, \tag{B.10}$$

and

$$-\frac{\partial}{\partial x}\hat{E}_z + \mathrm{j}\omega\mu\hat{H}_y = 0 \tag{B.11}$$

while outside the scatterer we have,

$$-\frac{\partial}{\partial x}\hat{H}_y + \frac{\partial}{\partial y}\hat{H}_x + \mathrm{j}\omega\epsilon\hat{E}_z = -\hat{J}_z^{\mathrm{ext}}, \tag{B.12}$$

$$\frac{\partial}{\partial y}\hat{E}_z + \mathrm{j}\omega\mu\hat{H}_x = 0, \tag{B.13}$$

and

$$-\frac{\partial}{\partial x}\hat{E}_z + \mathrm{j}\omega\mu\hat{H}_y = 0. \tag{B.14}$$

Subtracting the background field form the total field equations and introducing the scattered field as

$$\hat{E}_{z;\mathrm{sc}} = \hat{E}_z - \hat{E}_{z;\mathrm{b}}, \quad \hat{H}_{x;\mathrm{sc}} = \hat{H}_x - \hat{H}_{x;\mathrm{b}}, \quad \text{and} \quad \hat{H}_{y;\mathrm{sc}} = \hat{H}_y - \hat{H}_{y;\mathrm{b}}, \tag{B.15}$$

we find that this scattered field satisfies the equations

$$-\frac{\partial}{\partial x}\hat{H}_{y;\mathrm{sc}} + \frac{\partial}{\partial y}\hat{H}_{x;\mathrm{sc}} + \mathrm{j}\omega\epsilon\hat{E}_{z;\mathrm{sc}} = -\hat{J}_{z;\mathrm{sc}}, \tag{B.16}$$

$$\frac{\partial}{\partial y}\hat{E}_{z;\mathrm{sc}} + \mathrm{j}\omega\mu\hat{H}_{x;\mathrm{sc}} = 0, \tag{B.17}$$

and

$$-\frac{\partial}{\partial x}\hat{E}_{z;\mathrm{sc}} + \mathrm{j}\omega\mu\hat{H}_{y;\mathrm{sc}} = 0, \tag{B.18}$$

where we have introduced the scattering source

$$\hat{J}_{z;\mathrm{sc}} = \begin{cases} 0 & \text{if } \mathbf{r} \notin \mathbb{D}_{\mathrm{obj}} \\ \left[\sigma + \mathrm{j}\omega\epsilon_0(\epsilon_r - 1)\right]\hat{E}_z(\mathbf{r}, w) & \text{if } \mathbf{r} \in \mathbb{D}_{\mathrm{obj}}. \end{cases} \tag{B.19}$$

Equations B.16-B.18 holds for all $\mathbf{r} \in \mathbb{R}^2$ and from these equations we obtain an equation for the electric field strength by first multiplying Equation B.16 by $j\omega\mu$, results in

$$-\frac{\partial}{\partial x}\mathrm{j}\omega\mu\hat{H}_{y;\mathrm{sc}} + \frac{\partial}{\partial y}\mathrm{j}\omega\mu\hat{H}_{x;\mathrm{sc}} - k_{\mathrm{b}}^2\hat{E}_{z;\mathrm{sc}} = -\mathrm{j}\omega\mu\hat{J}_{z;\mathrm{sc}}, \tag{B.20}$$

where we used $c^2 = 1/(\epsilon\mu)$ and $k_{\mathrm{b}} = \omega^2/c^2$. Subsequently, substituting Equations B.17 and B.18, we get

$$\left(\frac{\partial}{\partial x^2} + \frac{\partial}{\partial y^2} + k_{\mathrm{b}}^2\right)\hat{E}_{z;\mathrm{sc}} = \mathrm{j}\omega\mu\hat{J}_{z;\mathrm{sc}}. \tag{B.21}$$

Now let $\hat{G}(\mathbf{r}, \omega)$ satisfy

$$\left(\frac{\partial}{\partial x^2} + \frac{\partial}{\partial y^2} + k_{\mathrm{b}}^2\right)\hat{G} = -\delta(\mathbf{r}), \tag{B.22}$$

where the delta function is the Dirac distribution operative at $\mathbf{r} = \mathbf{0}$. In addition, let $\hat{G}$ satisfy the radiation condition at infinity. Obviously, $\hat{G}$ is the scalar Green's function for our homogeneous background medium. An expression for $\hat{G}$ will be presented below.

Given this Green's function $\hat{G}$, the scattered electric field strength is given by

$$\hat{E}_{z;\mathrm{sc}}(\mathbf{r}, \omega) = \mathrm{j}\omega\mu \int_{\mathbf{r}' \in \mathbb{D}_{\mathrm{obj}}} \hat{G}(\mathbf{r} - \mathbf{r}', \omega)\hat{J}_{z;\mathrm{sc}}(\mathbf{r}', \omega)dA. \tag{B.23}$$

This integral representation holds for any $\mathbf{r} \in \mathbb{R}^2$. Using the definition of the scattering source, the above result can be written as

$$\hat{E}_{z;\mathrm{sc}}(\mathbf{r}, \omega) = k_{\mathrm{b}}^2\hat{A}(\mathbf{r}, \omega), \quad \forall \mathbf{r} \in \mathbb{R}^2, \tag{B.24}$$

where we have introduced the vector potential as

$$\hat{A}(\mathbf{r},\omega) = \int_{\mathbf{r}'\in\mathbb{D}_{\text{obj}}} \hat{G}(\mathbf{r}-\mathbf{r}',\omega)\hat{\chi}(\mathbf{r}',\omega)\hat{E}_z(\mathbf{r}',\omega)dA, \tag{B.25}$$

and $\hat{\chi}$ is the contrast function defined as

$$\hat{\chi}(\mathbf{r}',\omega) = \epsilon_r(\mathbf{r}) - 1 - \mathrm{j}\frac{\sigma(\mathbf{r})}{\omega\epsilon_0}. \tag{B.26}$$

If we restrict the observation vector to the scattering domain, then Equation B.24 becomes an integral equation for the total electric field strength inside the scatterer, Written out in full, we have

$$\hat{E}_z(\mathbf{r}',\omega) - k_{\text{b}}^2 \int_{\mathbf{r}'\in\mathbb{D}_{\text{obj}}} \hat{G}(\mathbf{r}-\mathbf{r}',\omega)\hat{\chi}(\mathbf{r}',\omega)\hat{E}_z(\mathbf{r}',\omega)dA = \hat{E}_{z;\text{b}}(\mathbf{r}',\omega), \quad \forall\mathbf{r}\in\mathbb{D}_{\text{obj}}. \tag{B.27}$$

This integral equation needs to be discretized to solve it for $\hat{E}_z$ on a computer. Therefore, let the scatterer occupy a rectangular domain with side length l_x in the x-direction and side length l_y in the y-direction. Furthermore, let the origin of our reference frame coincide with the upper left corner of the scattering domain as indicated in Figure B.1.

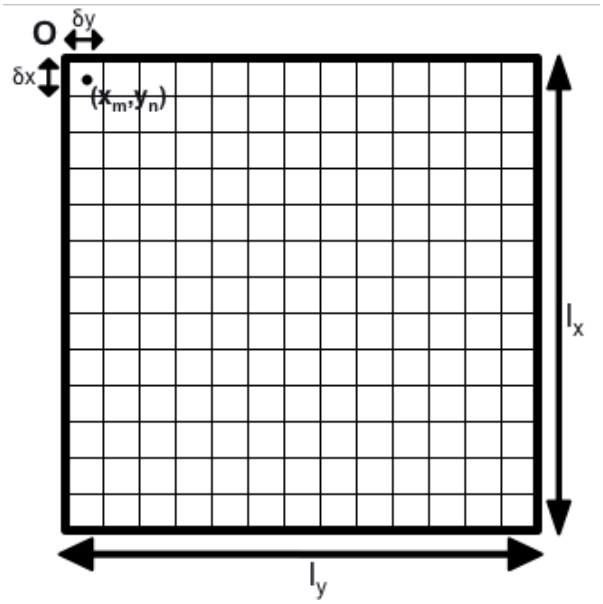

Figure B.1: The uniform grid used for the discretization, where the number of grid cells (MN) with middle point (x_m, y_n) can vary depending of the size on the grid and the size of each grid cell.

We introduce the grid coordinates

$$x_m = \frac{\delta x}{2} + m\delta x \quad \text{for} \quad m = 1,2,\dots,M, \tag{B.28}$$

with $\delta x = l_x/M$, and

$$y_n = \frac{\delta y}{2} + n\delta y \quad \text{for} \quad n = 1,2,\dots,N, \tag{B.29}$$

with $\delta y = l_y/N$.

The scattering domain is divided into discretization cells

$$S_{ij} = \left\{ i\delta x < x < (i+1)\delta x \quad , \quad j\delta y < y < (j+1)\delta y \right\} \tag{B.30}$$

for $i = 1,2,\dots,M$ and $j = 1,2,\dots,N$. Obviously, these cells do not overlap and the total number of cells is MN.

Let us start with Equation B.24 (repeated here for convenience), where the observation vector is placed in the scatterer

$$\hat{E}_{z;\mathrm{sc}}(\mathbf{r},\omega) = k_{\mathrm{b}}^2 \hat{A}(\mathbf{r},\omega), \quad \forall \mathbf{r} \in \mathbb{D}_{\mathrm{obj}}, \tag{B.31}$$

We require that this equation holds for all grid points located within the scatterer. Dropping the ω-dependence in our notation, we have

$$\hat{E}_{z;\mathrm{sc}}(x_m, y_n) = k_{\mathrm{b}}^2 \hat{A}(x_m, y_n), \tag{B.32}$$

for $m = 1, 2, \ldots, M$ and $n = 1, 2, \ldots, N$. We can simplify this by introducing a matrix notation

$$\mathbf{E}_z - k_{\mathrm{b}}^2 \mathbf{A} = \mathbf{E}_{z;\mathrm{b}}, \tag{B.33}$$

with matrices $\mathbf{E}_z$, $\mathbf{E}_{z;\mathrm{b}}$, and $\mathbf{A}$ as

$$(\mathbf{E}_z)\big|_{mn} = \hat{E}_z(x_m, y_n) \qquad \begin{matrix} m = 1, 2, \ldots, M \\ n = 1, 2, \ldots, N \end{matrix} \tag{B.34}$$

$$(\mathbf{E}_{z;\mathrm{b}})\big|_{mn} = \hat{E}_{z;\mathrm{b}}(x_m, y_n) \qquad \begin{matrix} m = 1, 2, \ldots, M \\ n = 1, 2, \ldots, N \end{matrix} \tag{B.35}$$

$$\mathbf{A} := \begin{pmatrix} \hat{A}(x_1, y_1) & \hat{A}(x_1, y_2) & \cdots & \hat{A}(x_1, y_N) \\ \hat{A}(x_2, y_1) & \hat{A}(x_2, y_2) & \cdots & \hat{A}(x_2, y_N) \\ \vdots & \vdots & \ddots & \vdots \\ \hat{A}(x_M, y_1) & \hat{A}(x_M, y_2) & \cdots & \hat{A}(x_M, y_N) \end{pmatrix} \tag{B.36}$$

Furthermore, we can use vector notation by applying the vec-operation as

$$\mathbf{e}_z = \mathrm{vec}(\mathbf{E}_z), \quad \mathbf{e}_{z;\mathrm{b}} = \mathrm{vec}(\mathbf{E}_{z;\mathrm{b}}), \quad \mathbf{a} = \mathrm{vec}(\mathbf{A}). \tag{B.37}$$

Finally, we can write Equation B.33 in vector notation

$$\mathbf{e}_z - k_{\mathrm{b}}^2 \mathbf{a} = \mathbf{e}_{z;\mathrm{b}}. \tag{B.38}$$

The only thing left is to relate the vector potential **a** to the electric field strength $\mathbf{e}_z$ using the definition of the vector potential. In continous form, the relation between the vector potential and the electric field strength is given by Equation B.25 (repeated here)

$$\hat{A}(\mathbf{r},\omega) = \int_{\mathbf{r}' \in \mathbb{D}_{\mathrm{obj}}} \hat{G}(\mathbf{r} - \mathbf{r}', \omega) \hat{\chi}(\mathbf{r}', \omega) \hat{E}_z(\mathbf{r}', \omega) dA, \tag{B.39}$$

where $\hat{G}$ is the Green's function satisfying Equation B.22 and the radiation condition. This function is given by

$$\hat{G}(\mathbf{r}, w) = -\frac{\mathrm{j}}{4} H_0^{(2)}(k_{\mathrm{b}}|\mathbf{r}|), \tag{B.40}$$

where $H_0^{(2)}$ is the Hankel function of the second kind and order zero.

Notice that with $\mathbf{r} \in \mathbb{D}_{\mathrm{obj}}$, the argument of the Green's function becomes zero when the integration vector **r**' is equal to **r**. We cannot discretize Equation B.39 in a straightforward manner, since the Hankel function has a logarithmic singularity at the origin.

A solution is to work with a so-called 'weak' Green's function instead of the original Green's function. This weakened Green's function satisfies

$$\left(\delta x^2 + \delta y^2 + k_{\mathrm{b}}^2\right) \hat{G}^w = -f(\mathbf{r}), \tag{B.41}$$

and the radiation condition at infinity. The function f has a bounded circular support $\mathbb{D}_{\mathrm{circ}}$ centered at the origin and is given by

$$f(\mathbf{r}) = \begin{cases} \frac{1}{\pi a^2} & \text{if } \mathbf{r} \in \mathbb{D}_{\mathrm{circ}}, \\ 0 & \text{if } \mathbf{r} \notin \mathbb{D}_{\mathrm{circ}}, \end{cases} \tag{B.42}$$

where $a = \frac{1}{2}\min\{\delta x, \delta y\}$ is the radius of the circular disc $\mathbb{D}_{\text{circ}}$. Note that

$$\int_{\mathbf{r}\in\mathbb{R}^2} f(\mathbf{r})dA = \frac{1}{\pi a^2}\int_{\mathbf{r}'\in\mathbb{D}_{\text{circ}}} dA = 1, \tag{B.43}$$

and f approaches the Dirac distribution when the radius of the circular disc goes to zero. The solution of Equation B.41 can now be written as

$$\begin{aligned}\hat{G}^w(\mathbf{r},\omega) &= \int_{\mathbf{r}'\in\mathbb{D}_{\text{circ}}} \hat{G}(\mathbf{r}-\mathbf{r}',\omega)f(\mathbf{r}')dA \\ &= \frac{1}{\pi a^2}\int_{\mathbf{r}'\in\mathbb{D}_{\text{circ}}} \hat{G}(\mathbf{r}-\mathbf{r}',\omega)dA \\ &= \frac{1}{4\pi a^2}\int_{\mathbf{r}'\in\mathbb{D}_{\text{circ}}} H_0^{(2)}(k_{\text{b}}|\mathbf{r}-\mathbf{r}'|,\omega)dA.\end{aligned} \tag{B.44}$$

After evaluating this integral outside the $\mathbb{D}_{\text{circ}}$ and at the center ($\mathbf{r} = \mathbf{0}$) of the disc, done in [20], we have

$$\hat{G}^w(\mathbf{r},\omega) = \begin{cases}\frac{-\text{j}}{2k_{\text{b}}a}\left[H_1^{(2)}(k_{\text{b}}a) - \frac{2\text{j}}{\pi k_{\text{b}}a}\right] & \text{if } \mathbf{r} = \mathbf{0}, \\ \frac{-\text{j}}{2k_{\text{b}}a}J_1(k_{\text{b}}a)H_0^{(2)}(k_{\text{b}}|\mathbf{r}|) & \text{if } \mathbf{r} \notin \mathbb{D}_{\text{circ}}.\end{cases} \tag{B.45}$$

Finally, with the above expression for the weakened Green's function we are able to discretize the vector potential

$$\hat{A}(\mathbf{r},\omega) = \int_{\mathbf{r}'\in\mathbb{D}_{\text{obj}}} \hat{G}^w(\mathbf{r}-\mathbf{r}',\omega)\hat{\chi}(\mathbf{r}',\omega)\hat{E}_z(\mathbf{r}',\omega)dA. \tag{B.46}$$

The vector potential $\hat{A}$ needs to be calculated at the grid nodes (x_m, y_n) $m = 1, 2 \ldots, M$ and $n = 1, 2, \ldots, N$. Introducing the position vector

$$\begin{aligned}\mathbf{r}_{mn} = x_m\mathbf{i}_x + y_n\mathbf{i}_y \quad & m = 1, 2, \ldots, M, \\ & n = 1, 2, \ldots, N.\end{aligned} \tag{B.47}$$

We write

$$\hat{A}(x_m, y_n) = \int_{\mathbf{r}'\in\mathbb{D}_{\text{obj}}} \hat{G}^w(\mathbf{r}_{mn}-\mathbf{r}')\hat{\chi}(\mathbf{r}')\hat{E}_z(\mathbf{r}')dA, \tag{B.48}$$

for $m = 1, 2, \ldots, M$ and $n = 1, 2, \ldots, N$ and we have dropped the ω-dependence of $\hat{A}$ as well. Furthermore, a piecewise constant contrast function is introduced, such that $\hat{\chi}$ is equal to a constant χ_{ij} in the discretization cell S_{ij}. Now, we can write

$$\hat{A}(x_m, y_n) = \sum_{i=1}^{M}\sum_{j=1}^{N}\chi_{ij}\int_{\mathbf{r}'\in\text{x}_{ij}} \hat{G}^w(\mathbf{r}_{mn}-\mathbf{r}')\hat{E}_z(\mathbf{r}')dA, \tag{B.49}$$

for $m = 1, 2, \ldots, M$ and $n = 1, 2, \ldots, N$. Finally, approximating the integral by the midpoint rule, we arrive at

$$\hat{A}(x_m, y_n) \approx \delta x\delta y\sum_{i=1}^{M}\sum_{j=1}^{N}\hat{G}^w(\mathbf{r}_{mn}-\mathbf{r}_{i,j})\chi_{ij}\hat{E}_z(\mathbf{r}_{ij})dA, \tag{B.50}$$

for $m = 1, 2, \ldots, M$ and $n = 1, 2, \ldots, N$. Using Equation B.45, we have

$$\hat{G}^w(\mathbf{r}_{mn}-\mathbf{r}_{i,j}) = \begin{cases}\frac{-\text{j}}{2k_{\text{b}}a}\left[H_1^{(2)}(k_{\text{b}}a) - \frac{2\text{j}}{\pi k_{\text{b}}a}\right] & \text{if } i = m \quad \text{and} \quad j = n, \\ \frac{-\text{j}}{2k_{\text{b}}a}J_1(k_{\text{b}}a)H_0^{(2)}(k_{\text{b}}|\mathbf{r}_{mn}-\mathbf{r}_{ij}|) & \text{if } i \neq m \quad \text{and} \quad j \neq n.\end{cases} \tag{B.51}$$

The discretized equation for the electric field strength can be given by introducing the contrast matrix

$$\mathbf{x} = \text{vec}(\chi_{ij}) \quad \text{and} \quad \mathbf{X} = \text{diag}(\mathbf{x}), \tag{B.52}$$

and matrices $\hat{\mathbf{G}}_{jn}, j, n = 1, 2, \ldots, N$, of order M with elements

$$(\hat{\mathbf{G}}_{jn})_{i,m} = \delta x \delta y \hat{G}^{w}(\mathbf{r}_{mn} - \mathbf{r}_{ij}), \tag{B.53}$$

with $i, m = 1, 2, \ldots, M$. Matrix $\mathbf{G}$ is now given by

$$\mathbf{G} = k_{\mathrm{b}}^2 \begin{pmatrix} \hat{\mathbf{G}}_{11} & \hat{\mathbf{G}}_{12} & \cdots & \hat{\mathbf{G}}_{1N} \\ \hat{\mathbf{G}}_{21} & \hat{\mathbf{G}}_{22} & \cdots & \hat{\mathbf{G}}_{2N} \\ \vdots & \vdots & \ddots & \vdots \\ \hat{\mathbf{G}}_{N1} & \hat{\mathbf{G}}_{N2} & \cdots & \hat{\mathbf{G}}_{NN} \end{pmatrix}. \tag{B.54}$$

It can easily be verified that matrix $\mathbf{G}$ is block Toeplitz and each block is a Toeplitz matrix as well. Furthermore, matrix $\mathbf{G}$ is symmetric (but not Hermitian) and all self patch elements are located on the diagonal. Now, the final result becomes

$$(\mathbf{I} - \mathbf{G}\mathbf{X})\mathbf{e}_z = \mathbf{e}_{z;\mathrm{b}}, \tag{B.55}$$

and this discretized integral equation can easily be with an iterative solver since the actions of $\mathbf{G}$ on a vector can be computed efficiently via FFT.

C

Gauss-Newton

To arrive at Newton-type updating schemes, we start with a Taylor expansion of the objective function. We have

$$F(\chi + \delta\chi) = F(\chi) + \mathbf{g}_\chi^T \delta\mathbf{z} + \frac{1}{2}\delta\mathbf{z}\mathbf{H}_\chi\delta\mathbf{z} + \text{higher order terms}, \tag{C.1}$$

where we have the objective function with distortion term $\delta\chi$ defined as

$$F(\chi + \delta\chi) = \frac{\left|\mathcal{K}\mathbf{E}^{\text{desired}} - \mathcal{K}\mathbf{E}(\chi + \delta\chi)\right|^2}{\left|\mathcal{K}\mathbf{E}^{\text{desired}}\right|^2}. \tag{C.2}$$

We can write $\mathbf{E}$ in the Sherman-Morrison-Woodbury form, as defined in Equation 2.11. This results in

$$\begin{aligned} F(\chi + \delta\chi) = \left|\mathcal{K}\mathbf{E}^{\text{desired}}\right|^{-2} &\left\{\mathcal{K}\mathbf{E}^{\text{desired}} - \mathcal{K}\left[\mathbf{e} + \mathbf{Z}(\mathbf{I} - (\chi + \delta\chi)\mathbf{S}^T\mathbf{Z})^{-1}(\chi + \delta\chi)\mathbf{S}^T\mathbf{e}\right]\right\}^H \\ &\left\{\mathcal{K}\mathbf{E}^{\text{desired}} - \mathcal{K}\left[\mathbf{e} + \mathbf{Z}(\mathbf{I} - (\chi + \delta\chi)\mathbf{S}^T\mathbf{Z})^{-1}(\chi + \delta\chi)\mathbf{S}^T\mathbf{e}\right]\right\}, \end{aligned} \tag{C.3}$$

by introducing a scaling factor $c = 2\left|\mathcal{K}\mathbf{E}^{\text{desired}}\right|^{-2}$ and $\mathbf{A} = \mathbf{I} - \chi\mathbf{S}^T\mathbf{Z}$ the objective function can be rewritten as

$$\begin{aligned} F(\chi + \delta\chi) = \frac{1}{2}c &\left\{\mathcal{K}\mathbf{E}^{\text{desired}} - \mathcal{K}\left[\mathbf{e} + \mathbf{Z}\left(\mathbf{A}\left(\mathbf{I} - \delta\chi\mathbf{A}^{-1}\mathbf{S}^T\mathbf{Z}\right)\right)^{-1}\left(\chi\mathbf{S}^T\mathbf{e} + \delta\chi\mathbf{S}^T\mathbf{e}\right)\right]\right\}^H \\ &\left\{\mathcal{K}\mathbf{E}^{\text{desired}} - \mathcal{K}\left[\mathbf{e} + \mathbf{Z}\left(\mathbf{A}\left(\mathbf{I} - \delta\chi\mathbf{A}^{-1}\mathbf{S}^T\mathbf{Z}\right)\right)^{-1}\left(\chi\mathbf{S}^T\mathbf{e} + \delta\chi\mathbf{S}^T\mathbf{e}\right)\right]\right\}. \end{aligned} \tag{C.4}$$

A Taylor expansion now gives

$$\begin{aligned} F(\chi+\delta\chi) = \frac{1}{2}c &\left\{\mathcal{K}\mathbf{E}^{\text{desired}} - \mathcal{K}\left[\mathbf{e} + \mathbf{Z}\left(\mathbf{I} + \delta\chi\mathbf{A}^{-1}S^T\mathbf{Z} + \delta\chi^2\left(\mathbf{A}^{-1}S^T\mathbf{Z}\right)^2 + \ldots\right)\mathbf{A}^{-1}\left(\chi\mathbf{S}^T\mathbf{e} + \delta\chi\mathbf{S}^T\mathbf{e}\right)\right]\right\}^H \\ &\left\{\mathcal{K}\mathbf{E}^{\text{desired}} - \mathcal{K}\left[\mathbf{e} + \mathbf{Z}\left(\mathbf{I} + \delta\chi\mathbf{A}^{-1}S^T\mathbf{Z} + \delta\chi^2\left(\mathbf{A}^{-1}S^T\mathbf{Z}\right)^2 + \ldots\right)\mathbf{A}^{-1}\left(\chi\mathbf{S}^T\mathbf{e} + \delta\chi\mathbf{S}^T\mathbf{e}\right)\right]\right\}, \end{aligned} \tag{C.5}$$

rearranging all terms up to and including second order, we have

$$\begin{aligned} F(\chi + \delta\chi) = \frac{1}{2}c\Big\{\mathcal{K}\mathbf{E}^{\text{desired}} - \mathcal{K}\Big[&\mathbf{e} + \chi\mathbf{Z}\mathbf{A}^{-1}\mathbf{S}^T\mathbf{e} + \delta\chi\left(\mathbf{Z}\mathbf{A}^{-1}\mathbf{S}^T\mathbf{e} + \chi\mathbf{Z}\mathbf{A}^{-1}\mathbf{S}^T\mathbf{Z}\mathbf{A}^{-1}\mathbf{S}^T\mathbf{e}\right) \\ &+ \delta\chi^2\left(\mathbf{Z}\mathbf{A}^{-1}\mathbf{S}^T\mathbf{Z}\mathbf{A}^{-1}\mathbf{S}^T\mathbf{e} + \chi\mathbf{Z}\left(\mathbf{A}^{-1}\mathbf{S}^T\mathbf{Z}\right)^2\mathbf{A}^{-1}\mathbf{S}^T\mathbf{e}\right)\Big]\Big\}^H\Big\{\ldots\Big\}. \end{aligned} \tag{C.6}$$

Furthermore, simplify the objective function by noticing that $\mathbf{E}(\chi) = \mathbf{e} + \chi\mathbf{Z}\mathbf{A}^{-1}\mathbf{S}^T\mathbf{e}$ and by introducing $\mathbf{J}$ as follows

$$\mathbf{J} = \mathbf{Z}\mathbf{A}^{-1}\mathbf{S}^T\mathbf{e} + \chi\mathbf{Z}\mathbf{A}^{-1}\mathbf{S}^T\mathbf{Z}\mathbf{A}^{-1}\mathbf{S}^T\mathbf{e}, \tag{C.7}$$

and $\mathbf{G}$ as follows

$$\mathbf{G} = \mathbf{Z}\mathbf{A}^{-1}\mathbf{S}^T\mathbf{Z}\mathbf{A}^{-1}\mathbf{S}^T\mathbf{e} + \chi\mathbf{Z}\left(\mathbf{A}^{-1}\mathbf{S}^T\mathbf{Z}\right)^2\mathbf{A}^{-1}\mathbf{S}^T\mathbf{e}, \tag{C.8}$$

so we get

$$F(\chi+\delta\chi) = \frac{1}{2}c\left\{\mathcal{K}\mathbf{E}^{\text{desired}} - \mathcal{K}\left[\mathbf{E}(\chi)+\delta\chi\mathbf{J}+\delta\chi^2\mathbf{G}\right]\right\}^H\left\{\mathcal{K}\mathbf{E}^{\text{desired}} - \mathcal{K}\left[\mathbf{E}(\chi)+\delta\chi\mathbf{J}+\delta\chi^2\mathbf{G}\right]\right\}, \quad \text{(C.9)}$$

where we can define the residual $\mathbf{r}(\chi) = \mathcal{K}\mathbf{E}^{\text{desired}} - \mathcal{K}\mathbf{E}(\chi)$, work out the multiplication and rearranging all terms up to and including second order again. This results in

$$F(\chi+\delta\chi) = F(\chi) - c\text{Re}\left[\delta\chi\mathbf{J}^H\mathbf{r}(\chi)\right] + \frac{1}{2}c\left|\delta\chi\right|^2\left|\mathbf{J}\right|^2 - c\text{Re}\left[\delta\chi^2\mathbf{G}^H\mathbf{r}(\chi)\right], \quad \text{(C.10)}$$

which is now in the same form as the general form given in Equation C.1. Furthermore, we can rewrite this equation by splitting the contrast χ in a real and imaginary part as follows

$$F(\chi_r+\delta\chi_r,\chi_i+\delta\chi_i) = F(\chi_r,\chi_i) + \mathbf{g}_\chi^T\delta\mathbf{z} + \frac{1}{2}\delta\mathbf{z}\mathbf{H}_\chi\delta\mathbf{z} + \text{higher order terms}. \quad \text{(C.11)}$$

The second term on the right-hand side of Equation C.10 can be compared with this general form by writing it in terms of a real and imaginary part of χ. By further exploring the actual pad parameters ϵ_r and σ this becomes

$$\begin{aligned}
-c\text{Re}\left[\delta\chi\mathbf{J}^H\mathbf{r}(\chi)\right] &= -c\left\{\delta\chi_r\text{Re}\left[\mathbf{J}^H\mathbf{r}(\chi)\right] + \delta\chi_i\text{Im}\left[\mathbf{J}^H\mathbf{r}(\chi)\right]\right\} \\
&= -c\left\{\delta\epsilon_r\text{Re}\left[\mathbf{J}^H\mathbf{r}(\chi)\right] + \delta\sigma\text{Re}\left[\frac{1}{j\omega\epsilon_0}\mathbf{J}^H\mathbf{r}(\chi)\right]\right\} \\
&= -c\text{Re}\left[\mathbf{a}\mathbf{J}^H\mathbf{r}(\epsilon_r,\sigma)\right]\delta\mathbf{m} = \mathbf{g}^T\delta\mathbf{m}, \quad \text{(C.12)}
\end{aligned}$$

where we use

$$\delta\mathbf{z} = \mathbf{a}\delta\mathbf{m}, \quad \text{(C.13)}$$

with $\delta\mathbf{z} = [\delta\chi_r,\delta\chi_i]^T$, $\delta\mathbf{m} = [\delta\epsilon_r,\delta\sigma]^T$ and

$$\mathbf{a} = \begin{pmatrix} 1 & 0 \\ 0 & \frac{1}{j\omega\epsilon_0} \end{pmatrix}.$$

For the third and fourth term on the right-hand side, we have

$$\begin{aligned}
\frac{1}{2}c\left|\delta\chi\right|^2\left|\mathbf{J}\right|^2 - c\text{Re}\left[\delta\chi^2\mathbf{G}^H\mathbf{r}(\chi)\right] &= \frac{1}{2}c\left[(\delta\chi_r)^2 + (\delta\chi_i)^2\right]\left|\mathbf{J}\right|^2 \\
&= \frac{1}{2}c\delta\mathbf{m}^H\mathbf{a}^H\mathbf{J}^H\mathbf{J}\mathbf{a}\delta\mathbf{m} \\
&= \frac{1}{2}\delta\mathbf{m}^H\mathbf{H}\delta\mathbf{m}, \quad \text{(C.14)}
\end{aligned}$$

where we have neglected the fourth term under the assumption that the first-order term (third term) will dominate the second-order term (fourth term) [11]. This assumption is justified when the residual term is small, so when the initial guess is close to the optimal value. This method is called the Gauss-Newton method.

Bibliography

[1] M. A. Bernstein, J. Huston, and H. A. Ward. Imaging artifacts at 3.0 t. *Journal of Magnetic Resonance Imaging*, 24(4):735–746, 2006.

[2] J. Bonnans, J. C. Gilbert, C. Lemaréchal, and C. A. Sagastizábal. *Numerical optimization: theoretical and practical aspects*. Springer Science & Business Media, 2006.

[3] W. M. Brink, A. M. A. van der Jagt, M. J. Versluis, B. M. Verbist, and A. G. Webb. High permittivity dielectric pads improve high spatial resolution magnetic resonance imaging of the inner ear at 7 t. *Investigative radiology*, 49(5):271–277, 2014.

[4] W. M. Brink, R. F. Remis, and A. G. Webb. A theoretical approach based on electromagnetic scattering for analysing dielectric shimming in high-field mri. *Magnetic resonance in medicine*, 2015.

[5] K. J. J Chang and I. R. Kamel. Abdominal imaging at 3t: Challenges and solutions. *Applied Radiology*, 39(10):22, 2010.

[6] A. Christ, W. Kainz, E. G. Hahn, K. Honegger, et al. The virtual family-development of surface-based anatomical models of two adults and two children for dosimetric simulations. *Physics in medicine and biology*, 55(2):N23, 2009.

[7] C. M. Collins, W. Liu, J. Wang, R. Gruetter, et al. Temperature and sar calculations for a human head within volume and surface coils at 64 and 300 mhz. *Journal of Magnetic Resonance Imaging*, 19(5):650–656, 2004.

[8] Christopher M Collins and Zhangwei Wang. Calculation of radiofrequency electromagnetic fields and their effects in mri of human subjects. *Magnetic resonance in medicine*, 65(5):1470–1482, 2011.

[9] P. De Heer, W.M. Brink, B.J. Kooij, and A.G. Webb. Increasing signal homogeneity and image quality in abdominal imaging at 3 t with very high permittivity materials. *Magnetic resonance in medicine*, 68(4):1317–1324, 2012.

[10] Anthony J Devaney. *Mathematical foundations of imaging, tomography and wavefield inversion*. Cambridge University Press, 2012.

[11] P.E. Gill, W. Murray, and M.H. Wright. *Practical Optimization*. Academic Press Inc., 1981.

[12] G. H. Golub and C. F. Van Loan. *Matrix computations*, volume 3. JHU Press, 2012.

[13] T. M. Habashy and A. Abubakar. A general framework for constraint minimization for the inversion of electromagnetic measurements. *Progress In Electromagnetics Research*, 46:265–312, 2004.

[14] K. Haines, N. B. Smith, and A.G. Webb. New high dielectric constant materials for tailoring the distribution at high magnetic fields. *Journal of Magnetic Resonance*, 203(2):323 – 327, 2010. ISSN 1090-7807.

[15] R. A. Horn and C. R. Johnson. *Matrix analysis*. Cambridge university press, 1990.

[16] J. Jin. *Electromagnetic analysis and design in magnetic resonance imaging*, volume Vol.1. CRC Press, 1999.

[17] T. Neuberger, V. Tyagi, E. Semouchkina, M. Lanagan, A. Baker, K. Haines, and A.G. Webb. Design of a ceramic dielectric resonator for nmr microimaging at 14.1 tesla. *Concepts in Magnetic Resonance Part B: Magnetic Resonance Engineering*, 33(2):109–114, 2008.

[18] J. Nocedal and S. Wright. *Numerical optimization*. Springer Science & Business Media, 2006.

[19] J. L. Prince and J. M. Links. *Medical imaging signals and systems*. Pearson Prentice Hall„ Upper Saddle River, N.J. :, 2006.

[20] R. Remis and E. Charbon. An electric field volume integral equation approach to simulate surface plasmon polaritons. *Advanced Electromagnetics*, 2(1):15–24, 2013.

[21] S. Rupprecht, C. T. Sica, S. Raffi, K. Seongtae, M. T. Lanagan, and Q. X. Yang. Drastic enhancement and manipulation of rf field with ultra high dielectric constant (uhdc) material at 3t. In *Proceedings of the 21st Annual Meeting of ISMRM, Salt Lake City, Utah, USA*, page 396, 2013.

[22] K. Setsompop, L.L. Wald, V. Alagappan, B.A. Gagoski, and E. Adalsteinsson. Magnitude least squares optimization for parallel radio frequency excitation design demonstrated at 7 tesla with eight channels. *Magnetic resonance in medicine*, 59(4):908–915, 2008.

[23] C. P. Slichter. *Principles of magnetic resonance*, volume 1. Springer Science & Business Media, 2013.

[24] M. Sreenivas, M. Lowry, P. Gibbs, M. Pickles, and L. W. Turnbull. A simple solution for reducing artefacts due to conductive and dielectric effects in clinical magnetic resonance imaging at 3 t. *European Journal of Radiology*, 62(1):143 – 146, 2007.

[25] W. M. Teeuwisse, W. M. Brink, K. N. Haines, and A. G. Webb. Simulations of high permittivity materials for 7 t neuroimaging and evaluation of a new barium titanate-based dielectric. *Magnetic Resonance in Medicine*, 67(4):912–918, 2012. ISSN 1522-2594.

[26] J. van Gemert, W. M. Brink, A. G. Webb, and R. F. Remis. An efficient high-permittivity pad design methodology for dielectric shimming in magnetic resonance imaging. *IEEE Transactions on Medical Imaging*, Submitted.

[27] A. G. Webb. Challenges for high field clinical mri. In *Proceedings of the 2010 IEEE international conference on Biomedical imaging: from nano to Macro*, pages 575–578. IEEE Press, 2010.

[28] S. A. Winkler and B. K. Rutt. Practical methods for improving b1+ homogeneity in 3 tesla breast imaging. *Journal of Magnetic Resonance Imaging*, 41(4):992–999, 2015.